Available online at www.sciencedirect.com

ScienceDirect

Geochimica et Cosmochimica Acta 286 (2020) 72–102

Geochimica et Cosmochimica Acta

www.elsevier.com/locate/gca

Fe-oxides in jasperoids from two gold districts in Nevada: Characterization, geochemistry, and (U-Th)/He dating

Dante E. Huff [a], Elizabeth Holley [b,*], William R. Guenthner [c], Jenna M. Kaempfer [c]

[a] Department of Geology and Geological Engineering, Colorado School of Mines, Golden, CO, USA
[b] Department of Mining Engineering, Colorado School of Mines, Golden, CO, USA
[c] Department of Geology, University of Illinois at Urbana-Champaign, Urbana, IL, USA

Received 6 January 2020; accepted in revised form 7 July 2020; Available online 16 July 2020

Abstract

This study examines the whole-rock geochemistry, Fe-oxide texture and crystal morphology, and Fe-oxide (U-Th)/He date variation of jasperoids, as well as the relationships between these characteristics, in order to evaluate jasperoids as an indicator for gold mineralization. Jasperoid samples with a range of textures, appearances, and expected gold concentrations were collected from two gold districts in Nevada: the northern Carlin trend (Gold Quarry Mine), and the Battle Mountain district (Marigold Mine; Battle Mountain prospect). In our jasperoid samples, whole-rock concentrations of Au are positively correlated with As, Ag, Pb, Sb, U, W, and Tl. The following Fe-oxide textures are associated with anomalous gold concentrations: disseminated, submicron crystals; feathery and acicular crystal morphologies; concentric zonation from hematite to goethite; and botryoidal textures. Calculated closure temperatures for the (U-Th)/He system in observed jasperoid Fe-oxide morphologies within our dataset range from 26 to 136 °C, indicating variable susceptibility to He diffusion at near-surface conditions. Fe-oxide (U-Th)/He dates range from 29.4 ± 0.5 Ma to 0.11 ± 0.01 Ma, displaying intra- and intersample variation. We attribute the date variation to multiple factors including He implantation, parent isotope exchange, and He loss through closure temperature sensitivity and alpha-ejection. The intra- and intersample variation within the Fe-oxide (U-Th)/He dates limits our ability to make geologic interpretations. Our case study identifies important limitations of the (U-Th)/He method in jasperoids and provides insight on how He date variation might be avoided in future studies.

Keywords: Jasperoids; Fe-oxide (U-Th)/He chronology; Carlin-type gold deposit

1. INTRODUCTION

The Carlin-type gold deposits (CTGDs) of northern Nevada (Fig. 1A) contain disseminated gold ore with major economic importance. CTGDs are replacement bodies in sedimentary host rocks, primarily silty carbonates, where Au occurs in solid solution with or as submicron particles in disseminated pyrite or marcasite (Hofstra and Cline, 2000; Cline et al., 2005). Although 90 Moz Au have been produced from deposits along the Carlin Trend (Fig. 1A; Muntean et al., 2018), exploration for CTGDs is challenging because the geochemical halos of the deposits do not extend far beyond the Au mineralized zones.

Jasperoid is one of the few CTGD alteration styles easily recognized at surface. The term "jasperoid" was first used by Spurr (1898) to describe silica replacement of pre-existing carbonates and other lithologies due to circulating fluid. Lovering (1972) defined jasperoid as "an epigenetic siliceous replacement of a previously lithified host rock," which is the definition we use hereafter. Silica precipitation and subsequent jasperoid alteration can occur under many conditions, however, jasperoid formation is most com-

* Corresponding author.
E-mail address: eholley@mines.edu (E. Holley).

https://doi.org/10.1016/j.gca.2020.07.014
0016-7037/

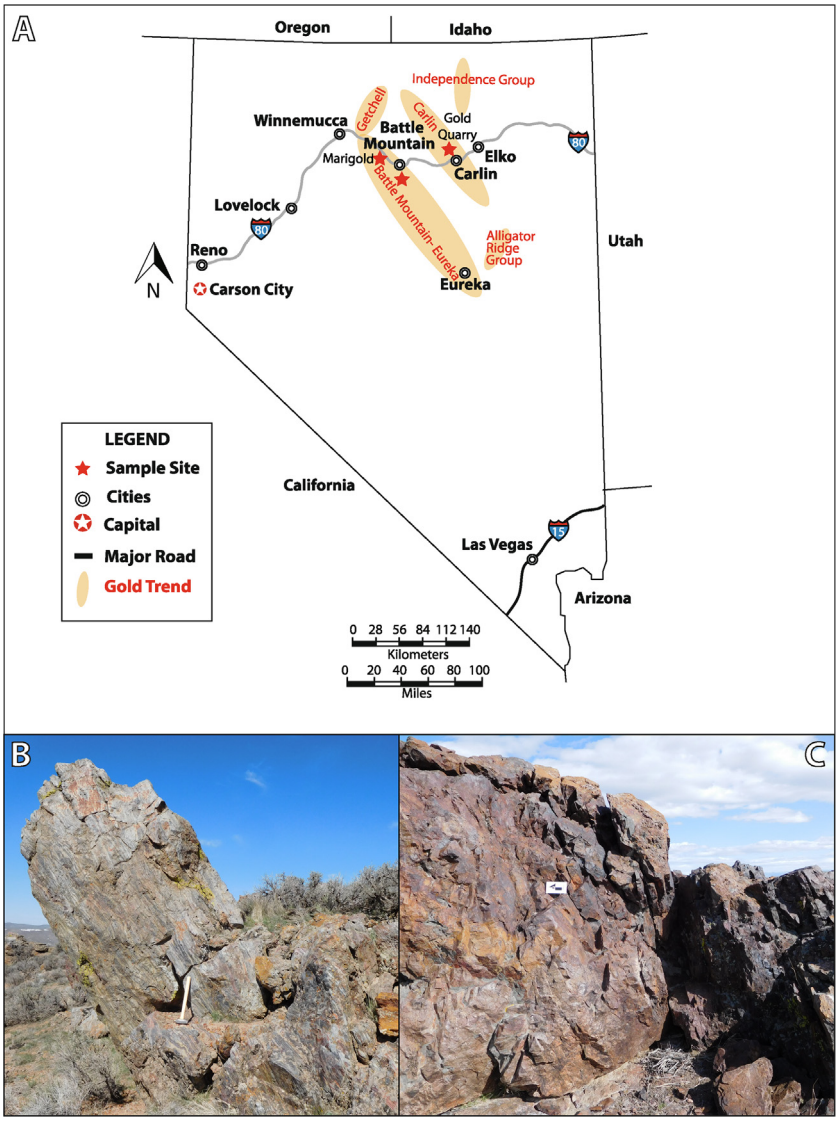

Fig. 1. Location map and outcrop photos from sample sites: (A) location map of Nevada with stars indicating sample locations; (B) facing northeast; representative photo of Gold Quarry sampling outcrop that highlights the prominent relief of jasperoid outcrops with respect to subcrop; (C) representative photo of Marigold sampling outcrop, facing east.

monly ascribed to hydrothermal fluid flow (Lovering, 1972). Jasperoid mineralogy is primarily silica and Fe-oxides; the Fe-oxides represent oxidation of any precursor Fe-bearing phase (Lovering, 1972). Resistive jasperoid outcrops at surface have long served as a prospecting tool in exploration for carbonate-hosted hydrothermal ore deposits such as CTGDs (Holland et al., 1988), but not every jasperoid forms from Au mineralizing fluids (Wells et al., 1969; Bakken and Einaudi, 1986; Cline et al., 2005). The Fe-oxides in CTGD jasperoids are thought to be secondary from the oxidation of ore-stage arsenian pyrite or other sulfides (e.g., Cline and Hofstra, 2000; Cline et al., 2005 and references therein). Carlin-type gold mineralization is generally thought to be Eocene (Chakurian et al., 2003; Cline et al., 2005; Ressel and Henry, 2006; Hickey et al., 2014; Fithian et al., 2018; Huff et al., 2018, 2019), but the age of the oxidation is unknown. Fe-oxide (U-Th)/He dating has been used to examine the timing of oxidized groundwater flow on the Colorado Plateau (Reiners et al., 2014), but the method has not been used to evaluate supergene processes in the Great Basin.

In this study, we examined Fe-oxides in jasperoids from three different locations in Nevada that are variably associated with known sedimentary rock-hosted Au mineralization: (1) the discovery outcrop for the Gold Quarry Mine on the northern Carlin trend, (2) outcropping jasperoids distal to the main ore zones at the Marigold Mine in the northern Battle Mountain district, and (3) a weakly mineralized prospect, also in the Battle Mountain district. In order to characterize Fe-oxide mineralogy and crystal morphology, we examined jasperoids in hand sample, as well as in thin section using optical petrography and scanning elec-

tron microscopy (SEM). We conducted bright phase searches using SEM-based automated mineralogy to determine whether native Au occurred in our samples. We combined these observations with whole-rock geochemistry to identify possible exploration indicators. The relatively simple mineralogy of jasperoids provided an opportunity to explore whether (U-Th)/He dating of Fe-oxides could reveal information about the geologic history of the gold deposits.

The (U-Th)/He dating method measures daughter He produced by the radioactive decay of naturally occurring U-Th within a mineral crystal lattice. Daughter He diffuses out of the crystal structure at higher temperatures and accumulates below an aliquot-specific closure temperature, T_c. Depending on the geologic context, thermal history, and T_c of the sample, the (U-Th)/He method may therefore provide either formation or thermal reset dates of the Fe-oxides (Ault et al., 2015, 2016; McDermott et al., 2017; Moser et al., 2017). We anticipated the Fe-oxide (U-Th)/He results would yield information in three possible categories: (1) different date populations between mineralized and unmineralized jasperoids could reflect physical and chemical differences in the secondary Fe-oxides; (2) the (U-Th)/He system might have captured the timing of oxidation, which would provide information on paleo-meteoric fluid migration in an area that presently lacks datasets; or (3) dates might represent the post-formation thermal history and paleotectonics of the sample locations. Instead, the intrasample dates showed intriguing variation that we hypothesize is not connected directly to any of these processes. Our detailed petrographic characterization of the Fe-oxides allows us to catalog the potential causes of the He date variation, including He implantation, parent isotope exchange, closure temperature sensitivity, and alpha-ejection. This assessment of open-system behavior demonstrates the limitations and challenges of applying the Fe-oxide (U-Th)/He chronometer to jasperoids.

2. BACKGROUND

In this section, we describe previous work that has been conducted on jasperoid prospectivity and Fe-oxide (U-Th)/He dating to highlight how our study examines different jasperoid characteristics and applies the Fe-oxide (U-Th)/He method in a novel context.

2.1. Previous research on jasperoids

Previously published studies on jasperoids focus on the whole-rock geochemistry and silica characteristics, at a single ore deposit or in one local area (Holland et al., 1988; Nelson, 1990; Theodore and Jones, 1991; Hofstra, 1994; Emsbo, 1999; Yigit et al., 2006). The emphasis on silica is due to the fact that many gold deposits display ore-stage silicification (Lovering, 1972; Bakken and Einaudi, 1986; Hofstra, 1994; Volk et al., 1995; Emsbo et al., 2003; Yigit et al., 2006). Numerous other ore deposit studies identified the presence of jasperoids without characterizing them (e.g., Wells et al., 1969; Sillitoe and Bonham, 1990; Rota and Hausen, 1991; Kuehn and Rose, 1992; Theodore et al., 1992; Hofstra, 1994; Hofstra et al., 2003; Cail and Cline, 2001; Cline et al., 2005 and references therein; Johnston et al., 2008). No prior studies have investigated the Fe-oxides, although their presence is commonly noted. Spurr (1898) recognized that variation in jasperoid color results from the presence of iron in different forms and proportions. Most jasperoids are oxidized and stained with Fe-oxides including goethite, hematite, and limonite (Lovering, 1972). In contrast to earlier research, this study focuses on jasperoid Fe-oxides in order to evaluate whether they serve as gold exploration indicators or reveal geologic processes which have affected CTGDs.

2.2. Fe-oxide (U-Th)/He dating

The (U-Th)/He method measures the He produced during alpha decay of naturally occurring U-Th radionuclides within crystal lattices. The diffusion kinetics of He are mineral-specific, and these kinetics can be used to calculate, with some key assumptions, a mineral-specific closure temperature. The simplest interpretation of a (U-Th)/He date, hereafter referred to as a He date, is therefore the amount of time since a crystal passed through its closure temperature (Zeitler et al., 1987). Closure temperature requires assumptions about sample cooling rate and a monotonic thermal history. For mineral systems where the diffusion domain is the crystal itself, closure temperature also varies with grain size, such that coarser grains correspond to higher closure temperatures (Reiners and Farley, 2001). In polycrystalline samples composed of variable grain sizes, He loss can occur over a spectrum of temperatures. Despite these complexities, closure temperature is a useful first-order approach to assess the relative temperature sensitivity among samples, and we use it as such throughout this manuscript. The partial retention zone (PRZ) is a more nuanced metric of temperature sensitivity, which we also use to contrast and compare the He diffusivities of our samples. As used in later sections, we define the PRZ here as the temperatures required for 0.1 and 0.9 fractional loss of He from a given sample for a set hold time. As with closure temperature, the PRZ is dependent on grain size, and this dependence will be a key focus in the discussion of our (U-Th)/He results. Helium loss can also occur through alpha-ejection, where radioactive decay of U-Th ejects a He daughter atom from the crystal lattice into the surrounding material, causing artificial younging of the apparent He date (Farley et al., 1996). Additional factors that may alter the He dates from their true values include: He implantation from interstitial mineral phases, parent isotope exchange, Fe-oxide mineralogy and morphology, and multiple Fe-oxide generations. We consider the influence of these factors on the He date variation in our dataset.

The Fe-oxide (U-Th)/He chronometer facilitates dating of geologic processes in settings that lack traditional (U-Th)/He chronometer minerals such as apatite and zircon. Strutt (1909) first investigated hematite as a U-He chronometer, but Lippolt et al. (1995) and Wernicke and Lippolt (1993, 1994a,b, 1997) were the first to apply the contemporary (U-Th)/He method to Fe-oxides. They interpreted their He dates to represent the formation age of the

iron ore deposits from which their samples came. Renewed interest in the Fe-oxide (U-Th)/He method comes from a better understanding of He diffusion kinetics, improved sampling procedures, and evidence that the method can produce He dates with geologically meaningful age interpretations. Recent studies have successfully used the Fe-oxide (U-Th)/He chronometer to investigate hydrothermal hematite formed on fault slip surfaces (Ault et al., 2015; McDermott et al., 2017), low-temperature cooling histories related to tectonics (Farley and Flowers, 2012; Evenson et al., 2014; Farley and McKeon, 2015; Calzolari et al., 2018) and oxide cements, fracture fills, and syntectonic mineralization produced by shallow water–rock redox interactions (Shuster et al., 2005; Monteiro et al., 2014; Reiners et al., 2014; Vasconcelos et al., 2015; Moser et al., 2017; Garcia et al., 2017). In these studies, Fe-oxide He dates were used to date the timing of oxide formation and the post-formation thermal history. The Fe-oxide (U-Th)/He chronometer has not been tested in economic geology, except for iron ore deposits (Lippolt et al., 1995; Wernicke and Lippolt, 1997, 1994, 1993; Heim et al., 2006; Danišík et al., 2013). This study examines whether the (U-Th)/He chronometer can be applied to jasperoid Fe-oxides in a mineral exploration context.

3. STUDY SITES

We collected nineteen jasperoid samples with a range of rock textures and Au concentrations from three sampling locations in Nevada: (1) the Gold Quarry Mine, (2) the Marigold Mine, and (3) prospective range-front jasperoid outcrops south of the town of Battle Mountain (Fig. 1A).

3.1. Gold Quarry

Gold Quarry is located along the northern Carlin Trend in Nevada. Three of the five jasperoid samples collected at Gold Quarry are from the mine's discovery outcrop (Fig. 1B), which lies along a major fault interpreted as a conduit for mineralizing fluids (Rota and Hausen, 1991). Existing geochronology and thermochronology data for the northern Carlin Trend suggest that hydrothermal activity and gold mineralization occurred primarily during the Eocene (Chakurian et al., 2003; Ressel and Henry, 2006; Hickey et al., 2014). We used samples from Gold Quarry as a benchmark to facilitate comparison of Fe-oxide characteristics from a known economically mineralized jasperoid, in comparison with unmineralized samples from other locations. The Gold Quarry samples also enabled us to test whether Fe-oxide (U-Th)/He date populations at the outcrop scale might reflect different episodes of oxidizing fluid flow along the fault.

3.2. Marigold Mine

The Marigold Mine exploits numerous sedimentary rock-hosted gold deposits in the Battle Mountain district of north-central Nevada. We collected jasperoid samples from several outcrops characterized as unmineralized by mine staff (Fig. 1C) and one outcrop described by Theodore (2000) as containing fifty times the background concentration of Au. We selected Marigold as a sampling location because a preliminary thermal history already exists for the Marigold deposits. Apatite fission track and apatite (U-Th)/He thermochronology data suggest that the most recent heating event at Marigold, interpreted to be the ore fluid event, occurred during the Late Eocene (Fithian et al., 2018; Huff et al., 2018, 2019).

3.3. Battle Mountain

There are no gold mines near the samples collected from range-front outcrops south of the town of Battle Mountain, but historic gold prospects exist in the area (Theodore and Jones, 1991). Those authors generated a geochemical dataset for jasperoids from this area, which provided an opportunity to assess the representivity of our jasperoid sampling. We sampled this area with the initial aim of testing the utility of jasperoid Fe-oxide characterization and (U-Th)/He analysis as tools to guide mineral exploration in an area distal to any known large gold deposits.

4. ANALYTICAL METHODS

4.1. Hand sample characterization

The workflow for hand sample characterization and subsequent analyses is documented in Fig. 2. Mineralogy, macroscopic texture, primary and secondary structures, and weathering were described in jasperoid hand samples, with special attention to oxidation features. These descriptions were used to determine categories of jasperoids with similar macroscopic features. A sample from each category was selected for later (U-Th)/He analysis to ensure a spectrum of Fe-oxide textures and relationships to Au were examined.

4.2. Optical petrography

A representative sample from each jasperoid category was selected for optical petrography. Thin sections were prepared at Spectrum Petrographics in Vancouver, Washington. Sample billets were embedded in clear resin, mounted with acrylic onto standard petrographic glass, and polished with 0.5 μm diamond abrasive to a final thickness of 100 μm. Samples were characterized in both transmitted and reflected light to determine mineralogy and to catalog distinctive Fe-oxide textures and morphologies.

4.3. Scanning electron microscopy

The jasperoid thin sections were examined by scanning electron microscopy (SEM) to characterize the microtextures of the Fe-oxides. Energy dispersive X-ray spectrometry (EDX) spot analyses provided semi-quantitative elemental concentrations, allowing for the identification of Fe-oxide mineral phases based on stoichiometry. Mineral phases likely to contain U-Th were also identified using stoichiometric calculations from EDX spot analyses. Energy dispersive X-ray spectrometry was also used to cre-

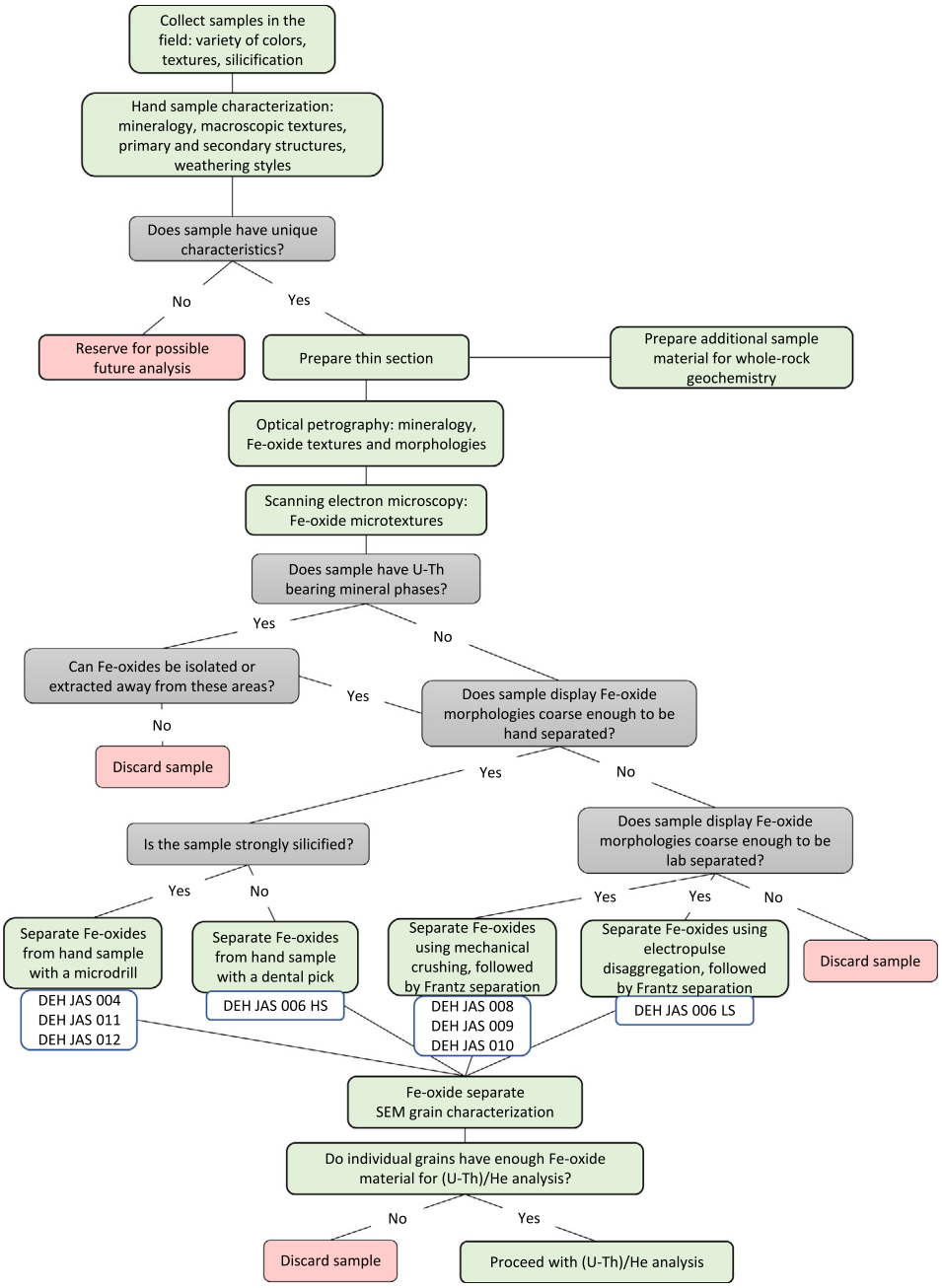

Fig. 2. Workflow diagram and decision tree detailing how jasperoid samples and Fe-oxide aliquots were selected and characterized prior to (U-Th)/He analysis.

ate element maps to determine the extent of silicification in the sample, to locate Fe-oxide phases, and to identify areas enriched in pathfinder elements for Au in CTGDs. Detailed methods are provided in Appendix A.

4.4. Geochemistry

Whole-rock geochemistry is the most common analytical method used in mineral exploration. During the early stages of a mineral exploration campaign, one or several grab samples are typically collected from outcrops demonstrating prospective alteration styles, such as jasperoid. Micron-scale geochemical methods, such as EDX spot analyses of thin sections, are reserved for more advanced exploration projects or may never be conducted at all. We collected whole-rock geochemical data to determine if particular jasperoid characteristics such as morphology or Fe-oxide (U-Th)/He dates might be associated with hand sample scale geochemical trends that are relevant for mineral exploration. In jasperoids, gold displays the nugget effect, where Au concentrations are highly localized; sampling and geochemical characterization at a small scale may miss

the presence of Au entirely (Nelson, 1990; Theodore and Jones, 1991; Dominy et al., 2003). A larger, bulk sample is more likely to record the occurrence of Au, allowing for a correlation between jasperoid and Fe-oxide characteristics and Au mineralization to be identified.

Whole-rock geochemical analyses for major oxides and 47 elements were conducted on splits of eighteen jasperoid samples by Activation Laboratories, Inc. (Actlabs) at their Ancaster, Ontario, Canada laboratory. Some elements were analyzed by multiple methods, depending on the expected concentration of the element and the detection limits of each laboratory method. The methods included fusion inductively coupled plasma-mass spectrometry (FICP-MS), instrumental neutron activation analysis (INAA), total digestion ICP-MS, and field ionization mass spectrometry (FIMS). Detailed methods are provided in Appendix A.

4.5. Bright phase search

We followed the rationale of Theodore and Jones (1991), who recommended that Au contents above 20 ppb should be considered anomalous for jasperoid samples in the Battle Mountain area. For our anomalous samples, we used an automated SEM-based bright phase search to characterize the gold deportment and to examine the microscopic textural relationship between anomalous gold and Fe-oxides. Samples were mapped with EDX with a beam spacing of 1 μm, due to the expected fine-grained nature of the Au. The EDX spectra at each acquisition point were compared with spectra held in a look-up table, allowing a mineral or phase to be assigned at each point. The bright phase search constituted analyses of points with a backscattered electron (BSE) brightness of at least 60%, which restricts the analyses to elements with a higher atomic Z number, including Au. This procedure generated a BSE map of all the acquisition points identified as gold. Details of the methods are presented in Appendix A.

4.6. Fe-oxide (U-Th)/He analysis

Several methods were used to separate Fe-oxides from the jasperoid whole-rock samples for (U-Th)/He analysis, including hand separation, crushing followed by Frantz separation, microdrilling, and electropulse disaggregation (EPD) followed by Frantz separation. Each of these methods is described in detail in Appendix A. Multiple separation methods were used to test whether different methods would isolate different styles of Fe-oxides. The Frantz separation step in the crushing and disaggregation (EPD) separation methods isolated concentrated Fe-oxide phases, such as vein fill. By contrast, the hand separation and microdrilling methods isolated both disseminated and concentrated Fe-oxides.

Following each separation method, representative aliquots were re-examined with the SEM to ensure that no U-Th bearing mineral phases other than Fe-oxide were present in the sample and to assess the ratio of Fe-oxide material to silica. After SEM screening, aliquots were selected from the mineral separate and their dimensions were measured and photographed using an optical microscope. A minimum of two aliquots from each sample were selected and packed in Nb envelopes for (U-Th)/He analysis performed at the University of Arizona. Analytical methods followed those described in Reiners et al. (2014) and are detailed in Appendix A.

No alpha-ejection corrections were applied for the Fe-oxide He dates because the aliquots were assumed to be part of an initial sample with dimensions larger than the alpha-stopping distance. This assumption is not valid for samples where there is more than 10% silica matrix and where individual Fe-oxide crystals <1 μm comprise the aggregates; the potential effect on He dates for such samples is addressed in the discussion.

4.7. Closure temperature calculations

Following the method of Calzolari et al. (2018), minimum, maximum, and mean half widths of Fe-oxide crystals were measured on SEM images in ImageJ to determine the possible effects of grain size distribution on temperature sensitivity. Plate half-widths were measured for platelet, bladed, and acicular morphologies. Crystal radii were measured for granular, spherical, anhedral, and aggregate morphologies. Once measurements were made for all Fe-oxide morphologies and jasperoid samples, closure temperatures were calculated using the closure temperature calculation of Dodson (1973) assuming a 10 °C/Myr cooling rate, as well as PRZ times and temperatures at 0.1 and 0.9 fractional loss. Both calculations used mineral-specific diffusion kinetics and aliquot-specific grain dimension measurements. For hematite grains, the activation energy of Farley and Flowers (2012) and D_0 of Evenson et al. (2014) were used. For goethite grains, the He diffusion kinetics of Shuster et al. (2005), Reiners et al. (2014), or Garcia et al. (2017) were used, depending on the Fe-oxide crystal morphology. Closure temperature and the PRZ were calculated to assess the relative temperature sensitivity of Fe-oxide grain sizes and different morphology populations within jasperoids, rather than the temperature below which no He diffusion occurs (Dodson, 1973; Braun et al., 2006). The closure temperature calculation and the numerical values of all standards and terms used are listed in Appendix A.

5. RESULTS

5.1. Jasperoid characterization

For each unique jasperoid category observed, we present a description of the hand sample, silica characteristics, and Fe-oxide characteristics (Table 1). The whole-rock Au concentration is provided for the analyzed sample split. The separation method used to isolate Fe-oxide aliquots and the He dates are provided for dated samples. Representative outcrop photos from Marigold and Gold Quarry are shown in Fig. 1B and C, respectively. Figs. 3 and 4 display hand sample photographs. Figs. 5 and 6 contain plane-polarized and reflected light photomicrographs from the

Table 1
Macro- and microscopic characteristics of jasperoids from Marigold, Battle Mountain, and Gold Quarry.

Sample ID	Hand sample description	Silica characteristics	Fe-oxide characteristics (morphology, size, spacing)	Au (ppb) DL[1]: 2 ppb
Marigold				
DEH JAS 002	Maroon, massive, homogeneous, exterior surface weathered to clay (Fig. 3A)	Fe-oxide stained quartz (Fig. 5A). Jigsaw quartz with grains 5–60 μm in diameter	Thin section shows sample is brecciated. Fe-oxide morphologies include: hematite platelet "books" (Fig. 7A), rounded grains, and wispy needles. Hexagonal hematite platelets (Fig. 7B) 5 μm wide and 100–500 nm thick, platelet aggregates are smaller than 65 μm, spacing between aggregates is 75–100 μm. Disseminated individual crystals are micron to submicron and spaced 10–30 μm apart	<2
DEH JAS 004	Dark brown, brecciated with barite cement, cherty, maroon veinlets (<1 mm) crosscut sample (Fig. 3B)	Fe-oxide stained quartz. Two generations of jigsaw quartz, distinguished by their birefringence and extinction orientations. More intense silicification along intragrain fractures	Fe-oxide morphologies include: hexagonal goethite platelets (Fig. 7C), needles, rounded, and anhedral grains. Individual crystals are submicron, but aggregates can reach up to 125 μm. A 100 μm thick surficial goethite rind shows colloform banding (Fig. 7D). The latest or exterior zone is 50 μm wide and appears brecciated in BSE imagery	<2
DEH JAS 006	Red, massive, with black, metallic veinlets (<1 mm; Fig. 3C)	Abundance of Fe-oxide staining and disseminated Fe-oxides obscures quartz in optical petrography (Fig. 5B). Silica occurs with abundant disseminated submicron granular and acicular Fe-oxides	Fe-oxides morphologies include: hexagonal and anhedral platelets, granular, acicular, and elongated to tabular goethite (Fig. 7E). Individual crystals measure 500 nm–20 μm long, with a length to width ratio of 10:1 at all scales. Irregular, branching goethite aggregates measuring over 500 μm long and 100 μm wide comprise the edges of the metallic veinlets visible in hand sample (Fig. 7F). Mn- and Mg-oxide species are also present in this sample	<2
DEH JAS 018	Dark greyish brown, sandstone with carbonate cement, variably silicified, crosscut by white opaque calcite and quartz veinlets (1–4 mm; Fig. 3D)	Fe-oxide stained quartz. Euhedral to subhedral, intergrown sedimentary quartz grains (50–100 μm) with up to 50% carbonate cement (Fig. 5C)	Mineralogy is 5% Fe-oxides. Fe-oxide morphologies include: subhedral and zoned cubic to pentagonal goethite crystals (5 μm) whose rims have grown together to form aggregates (Fig. 7G). Aggregates can approach lengths of 75 μm. In aggregates where individual goethite crystals cannot be distinguished, the internal texture appears brecciated (Fig. 7H), similar to the goethite rim observed in DEH JAS 004 (Fig. 7D)	<2
DEH JAS 018.2	Brown sandstone with calcite, quartz, and oxide veinlets (1–3 mm; Fig. 3E)	Subhedral to anhedral sedimentary quartz (50 μm). Recrystallized or re-cemented to jigsaw quartz, with interlocking anhedral quartz grains (5–10 μm)	Mineralogy is 30–35% oxide minerals (Fig. 5D). Rhomboid replacement texture (Fig. 5E). Goethite morphologies include: aggregates of spherical cores with cubic to pentagonal rims (Fig. 8A), disseminated blebs with acicular fringes (Fig. 8B), and rims on angular, shreddy Mn-oxide crystals with acicular to bladed edges (Fig. 8C). Fe-Mn, Mn-, and Ti-oxide species are also present in this sample (Fig. 8D)	7

(*continued on next page*)

Table 1 (*continued*)

Sample ID	Hand sample description	Silica characteristics	Fe-oxide characteristics (morphology, size, spacing)	Au (ppb) DL[1]: 2 ppb
Battle Mountain				
DEH JAS 008	Dark brown to dark reddish brown, massive cherty jasperoid with a distinct pale pink and white rim (Fig. 4F). Shows dissolution vugs (1 mm) throughout. Contains reactive fossil fragments of shells, corals, and crinoids (Fig. 6F)	Mineralogy is 70% quartz. Recrystallized to jigsaw quartz (1–15 μm). Heavily Fe-oxide stained	Mineralogy is 25% oxides. Opaque Mn-oxide (pyrolusite) veinlets (30–200 μm wide) contain individual crystals <5 μm in length with plate and acicular morphologies. Disseminated Fe-oxide aggregate morphologies include: spherical goethite nodules (Fig. 8E) similar to Fe-Mn-oxide nodules in DEH JAS 018-2 (Fig. 8D), shreddy, acicular, and blocky. Aggregates are <50 μm in diameter, and occur on the centimeter scale within the matrix. Shreddy Ti-oxides (30 μm) with dissolution textures and anhedral Cr-oxides (50 μm) are also present in this sample	14
DEH JAS 009	Mottled dark maroon to brown, cherty jasperoid. Contains fossil fragments of shells, corals, and crinoids (Fig. 7A)	Rounded to subrounded siltstone grains (1 mm) encircled by jigsaw quartz cement (1–15 μm) grains. Quartz cement is heavily oxide stained and contains calcite + barite grains	Fe-oxides occur as widely disseminated aggregates. Fe-oxide morphologies of individual crystals (<5 μm) include: acicular, shreddy, spherical, and plate. Possible fossil replacement textures (Fig. 8F). Aggregates are <50 μm in diameter and occur on the centimeter scale within the matrix. Individual Mn-oxide crystals are wispy (Fig. 8G) and rare Mn-oxide veinlets (30–200 μm wide) have "books" of platy crystals (Fig. 8H). Rare Ag-oxides and Ti-oxides with dissolution textures present	N/A
DEH JAS 010	Light brown to pink, massive, fine-grained calcareous grainstone. Calcite and Fe-oxide veinlets <1 mm crosscut sample	Trace silica grains. Unsilicified carbonate	Fe-oxides occur as disseminated grains and veinlet fill. Disseminated Fe-oxides resemble platy "books" of material less than 50 μm in diameter and are spaced hundreds of microns apart. Veinlet Fe-oxides occur as jumbled aggregates of polygonal plates, interspersed with blocky carbonate and barite grains	11
Gold Quarry				
DEH JAS 011	Intensely brecciated, silicified, laminated siltstone. Red oxidized siliceous matrix with angular breccia clasts (5 mm to 4 cm) that range in color from brownish grey to yellowish brown to maroon (Fig. 5A). Barite veinlets (<1mm) crosscut the sample	Submicron reticulated quartz. Mineralogy is 95% silica. Variable Fe-oxide staining changes color from dark brown to transparent. Jigsaw quartz in late stage qtz veins is coarser grain than matrix (25 μm)	Disseminated dark reddish brown Fe-oxides range in size from 1 μm to 300 μm (Fig. 6B). Acicular crystals (1 μm) with occur individually and as tightly packed, irregularly shaped aggregates up to 5 μm-wide. Spacing between disseminated individual oxide crystals is 2 μm, between aggregates 20 μm. A goethite surface rind 200–600 μm thick contains botryoidal and massive goethite (Fig. 9A), both of which show pitting. Rimming the massive goethite. In void spaces between botryoidal goethite are pockets of acicular goethite crystals, with an Sb signature, that can reach lengths of 4 μm (Fig. 9B)	101

DEH JAS 012	A blocky, siliceous, brown to purplish red, thinly laminated siltstone. Diffuse patches of orange to dark red oxidation (Fig. 5B, C)	Mineralogy is 90% silica. The siltstone is 1–20 μm jigsaw quartz grains. Quartz veins have coarser crystals (50–100 μm). One vein is rimmed by comb quartz with oscillatory extinction. Jigsaw quartz (1–5 μm) in the vein interior (Fig. 7C)	In optical petrography, Fe-oxides occur as disseminated spherical aggregates of granular crystals and as botryoidal aggregates (Fig. 6D) that rim quartz veins. Fe-oxides visible in BSE imagery are primarily disseminated acicular goethite crystals (2 μm) that form stars and crosses (Fig. 9C) and radiating acicular spherules (1.5 μm). Spacing between individual crystals ranges from 1 to 25 μm. One instance of acicular goethite crystals (<1 μm long) outlining a botryoidal shape (Fig. 9D), possibly rimming botryoidal silica indistinguishable in BSE imagery	140
DEH JAS 013	Dark reddish brown, cherty, laminated, with maroon veinlets and veins (<1–5 mm) that crosscut each other (Fig. 4D)	Mineralogy is 90% silica and remainder is disseminated oxides. Uniform, reticulated, 1–20 μm quartz grains	Dark reddish brown Fe-oxides occur as individual rounded or anhedral grains (1–5 μm) or as aggregates (20 μm). Aggregates weakly parallel primary bedding. No veinlets present in BSE imagery, suggesting the "veinlets" observed in hand sample are zones of iron-staining or disseminated oxides. All individual goethite crystals are submicron. The coarsest goethite aggregate observed is approximately 7 μm wide and consists of 75% acicular and 25% blocky crystals (Fig. 9E)	63
DEH JAS 014	Brown to maroon, highly silicified, massive siltstone. Brecciated section contains euhedral to angular barite clasts (<1 mm–5 cm) and unoxidized siltstone clasts (Fig. 4E). Dissolution vugs (<1–1 mm)	Mineralogy is 50% quartz. Jigsaw quartz grains 2–40 μm. Oscillatory extinction suggestive of grain boundary migration recrystallization	In optical petrography, individual Fe-oxides are dark red, but concentrate to form black, opaque aggregates. Aggregate distribution resembles snowflake obsidian (Fig. 6E). Aggregates are coarse (100–400 μm). Fe-oxide morphologies include: shreddy, anhedral, and tabular. Individual crystals range in size from 2 to 50 μm. Shreddy goethite crystals show possible dissolution textures (Fig. 9F). Fine anhedral crystals (10 μm) show hematite core and goethite rim zonation (Fig. 9F inset)	27
DEH JAS 015	Finely laminated, cherty, black and cream siltstone to mudstone. Colored bands of oxidation (1–3 cm thick) crosscut bedding at 60°, staining the protolith brown, yellow, and maroon (Fig. 4F)	Intensely silicified. Mineralogy dominated by jigsaw quartz (1–60 μm). Extensive pale brown to maroon staining due to disseminated submicron Fe-oxides (Fig. 6F)	Sinuous maroon oxide banding (20 μm–3 mm) is composed of very fine (1–10 μm) bladed and rounded Fe-oxide crystals disseminated in silica, with trace spherical Ti-oxide crystals. Oxide crystals are spaced 5–10 μm apart. Brecciated and deformed siltstone clasts within the oxide bands. Oxide aggregate abundance controls translucency of banding	3

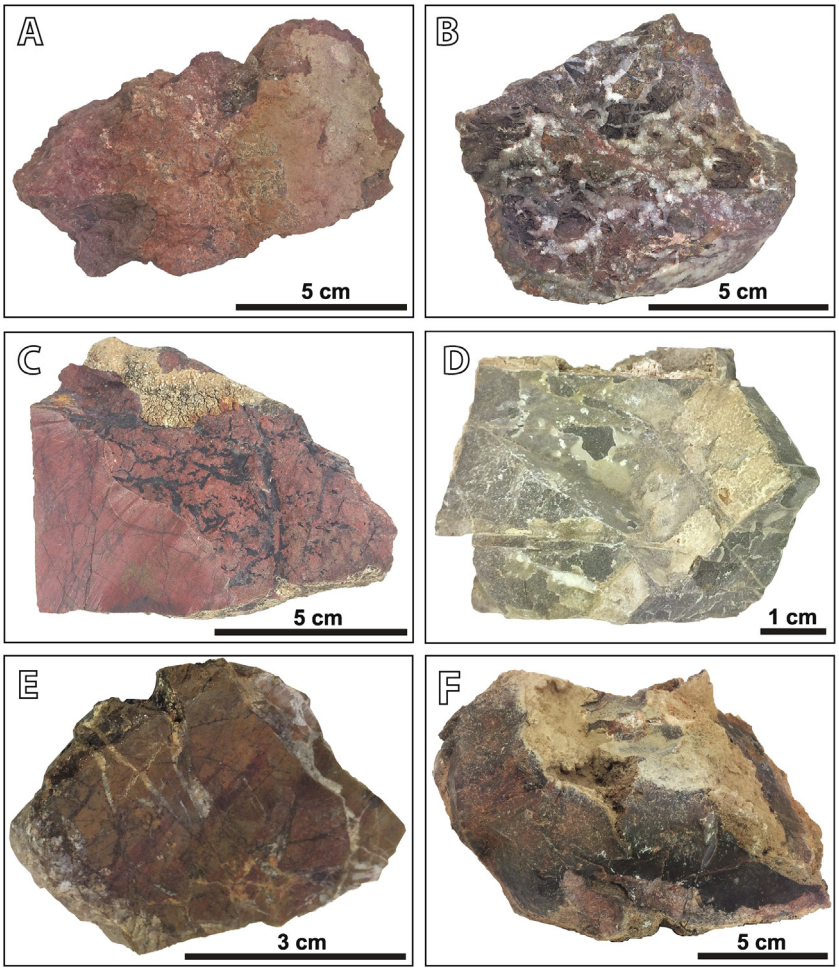

Fig. 3. Unique hand sample jasperoid categories from Marigold and Battle Mountain: (A) DEH JAS 002 – massive maroon jasperoid with moderate clay development; (B) DEH JAS 004 – brecciated jasperoid with barite infill; (C) DEH JAS 006 – massive red jasperoid with black, metallic veinlets; (D) DEH JAS 018 – dark greyish brown sandstone with carbonate cement, variably silicified, crosscut by white opaque calcite and quartz veinlets; (E) DEH JAS 018.2 – brown sandstone with calcite, quartz, and oxide veinlets from same outcrop as previous sample, showing stronger silicification; (F) DEH JAS 008 – dark brown to dark reddish brown, massive cherty jasperoid with a distinct pale pink and white rim. (For interpretation of the references to color in this figure legend, the reader is referred to the web version of this article.)

corresponding thin sections. Figs. 7–9 contain BSE images of Fe-oxide crystal morphologies and microtextures.

In hand sample, jasperoid colors are generally shades of brown and red. Silica occurs as jigsaw quartz and less commonly as quartz veining (Fig. 6C). The photomicrographs and BSE images reveal that the characteristic intense dark red and brown jasperoid colors, although suggestive of high oxide content, can actually result from widely disseminated and fine-grained oxides, with few oxide veinlets (Fig. 5D–F; Figs. 6B; 7F; 9C). Scanning electron microscopy reveals that areas which appear concentrated in oxides in hand sample or under the optical microscope, such as veins (Fig. 3B, C, E; Fig. 4A, B, D), laminations (Fig. 4B, D), and banding (Figs. 4D; 6F), are largely Fe-oxide stained silica and disseminated oxides. The apparent discrepancy between oxide concentrations at different scales may be the result of disseminated oxides present internally within the sample beneath the plane of SEM analysis but visible through translucent silica in optical petrography.

The Fe-oxide mineralogy is predominantly goethite and hematite. Other oxides observed in BSE images include Mn-oxide, Mg-oxide, Ti-oxide, and rare Cr- and Ag-oxides (Figs. 7F, 8B, C, D, F, H). Stoichiometry from the EDX spot analyses did not agree with common mineral species, likely because the analytical volume encompasses more than one grain. Fe-oxide crystals display a wide variety of morphologies, even within single samples (Table 1). Fe-oxide characteristics associated with gold-bearing samples are submicron acicular crystals (Fig. 9B, C, E), chemical zonation (Fig. 9F), and dissolution textures (Fig. 9A, F).

5.2. Geochemistry

Complete geochemistry results are included in Appendix B, and Au concentrations are reported in Table 1. Jasperoid samples from Marigold are below the detection limit for Au with the exception of one sample that contains 7 ppb Au,

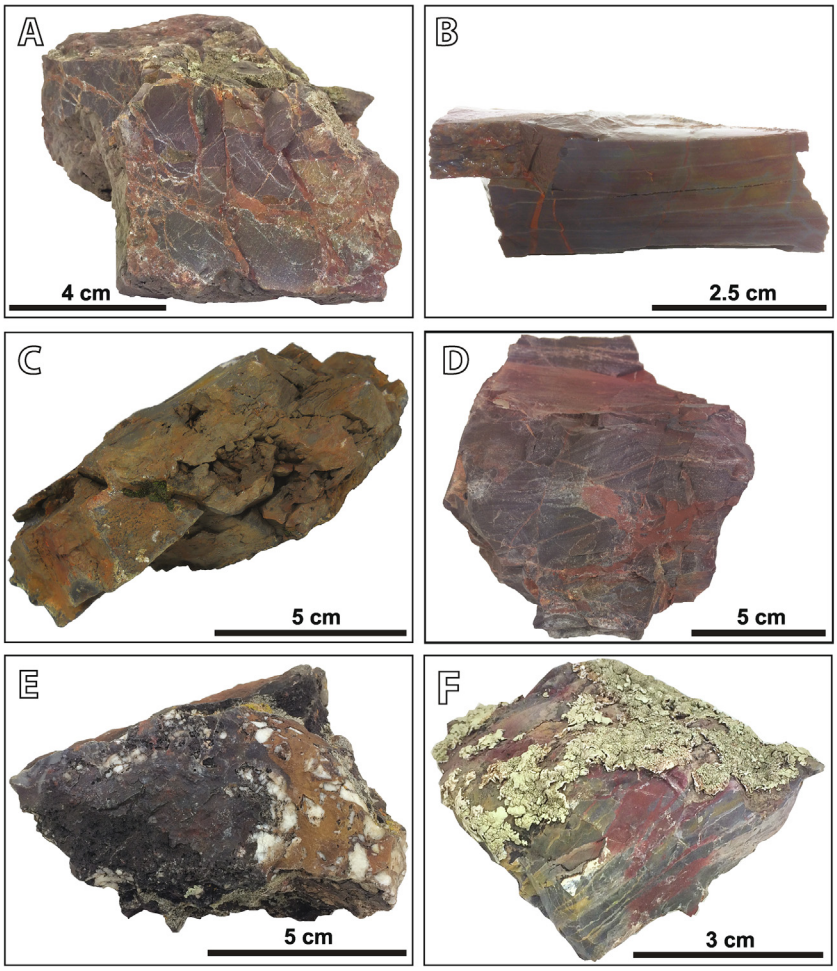

Fig. 4. Unique hand sample jasperoid categories from Gold Quarry: (A) DEH JAS 011 – intensely brecciated, silicified, laminated siltstone; (B) DEH JAS 012 – blocky, siliceous, brown to purplish red, thinly laminated siltstone; diffuse patches of orange to dark red oxidation; (C) DEH JAS 012 – blocky weathering surface of previous sample with dissolution; (D) DEH JAS 013 – dark reddish brown, cherty, laminated jasperoid with crosscutting maroon veinlets and veins; (E) DEH JAS 014 – brown to maroon, highly silicified, massive siltstone with fault breccia; (F) DEH JAS 015 – finely laminated, cherty, black and cream siltstone to mudstone with colored bands of oxidation that crosscut bedding. (For interpretation of the references to color in this figure legend, the reader is referred to the web version of this article.)

which is below background level for the area (Theodore and Jones, 1991; Theodore, 2000). Jasperoid samples from Battle Mountain are below background level (11 ppb and 14 ppb Au), whereas four samples from the Gold Quarry mine property are elevated (27–140 ppb Au). During the SEM-based automated mineralogy bright phase search, only one 2 μm long botryoidal aggregate of native gold was found (Fig. 10A). The only other minerals the bright phase search identified are single occurrences of cuprite, titanowodginite (a Ti-Ta oxide mineral), and an unknown Cu-Sn mineral.

The eighteen samples analyzed with whole-rock geochemistry are too small a dataset for robust statistical manipulation, but we can identify general trends. Table 2 highlights the Spearman correlation coefficients of the indicator elements identified by this study and earlier authors. A 1 or −1 indicates a complete positive or negative monotonic element variance and 0 indicates no correlation. Of the elements indicative of Au mineralization identified by previous jasperoid studies (Lovering, 1972; Holland et al., 1988; Nelson, 1990; Theodore and Jones, 1991; Yigit et al., 2006), in our dataset As, Pb, Sb, Tl, and W show a strong positive correlation with Au ($\geq$0.75), and Ag shows a moderate correlation (0.66; Table 2). All remaining elements display correlations that are too weak to be described as significant ($\leq$0.50). Unlike prior studies, in our dataset U displays a strong correlation with Au (0.78).

A Spearman correlation table of all geochemistry results (Appendix B) shows trends that align with alteration styles. Silica shows a weak negative correlation (−0.33) with CaO. Total iron as Fe_2O_3 shows a strong negative correlation (−0.84) with CaO. These correlations reflect the silica and iron replacement of carbonate and subsequent oxidation typical of jasperoid alteration. Potassium and aluminum show a nearly perfect positive correlation (0.97). Sodium shows a strong positive correlation with both potassium

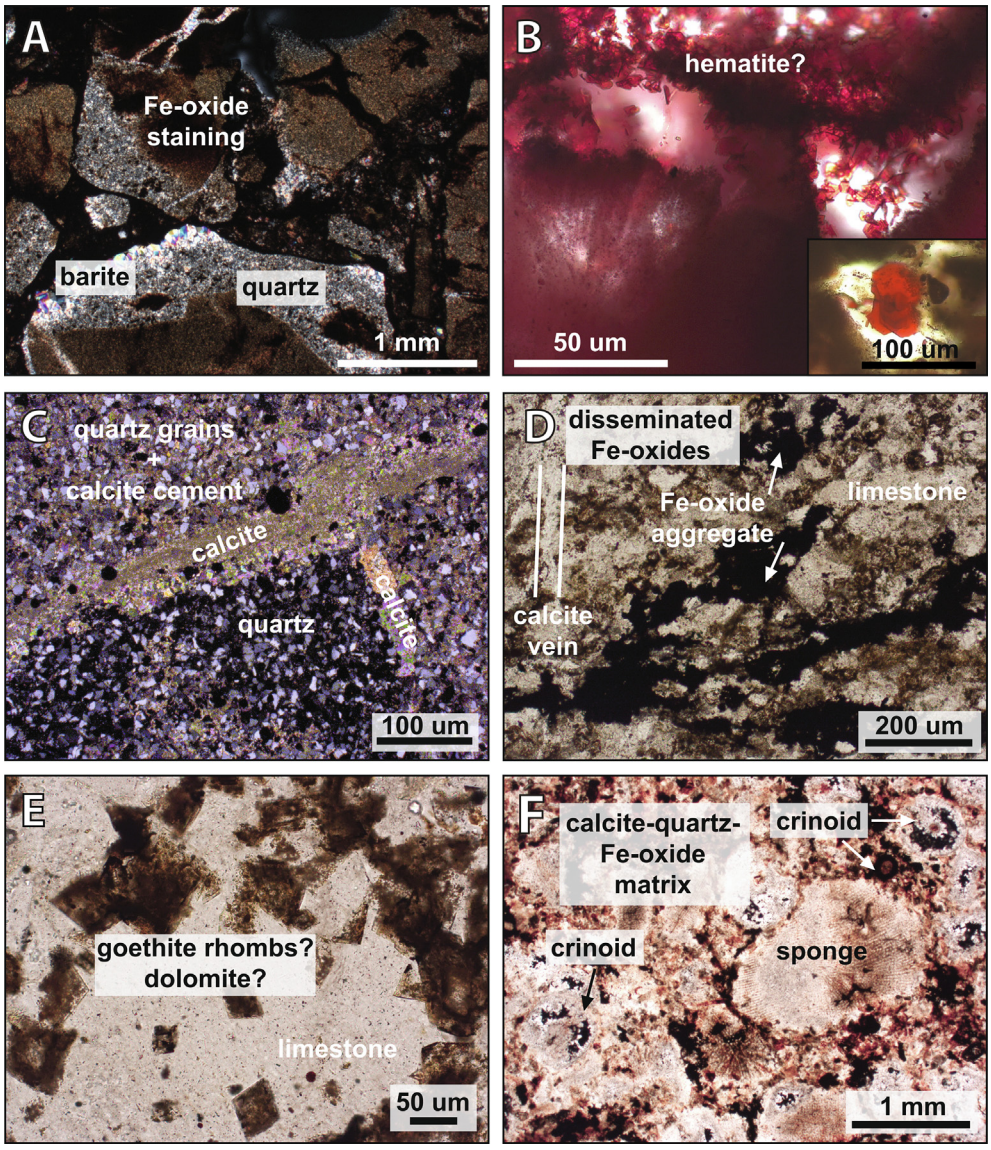

Fig. 5. Photomicrographs of silica and Fe-oxide textures from Marigold and Battle Mountain samples: (A) DEH JAS 002 – siliciclastic breccia clasts with Fe-oxide staining in interior and Fe-oxide breccia fill in cross-polarized light (XPL); barite displays comb texture; (B) DEH JAS 006 – translucent red hexagonal hematite platelets with micron-scale disseminated Fe-oxide crystals in a radiating pattern in plane-polarized light (PPL); see inset for magnified view of hematite platelet; (C) DEH JAS 018 – zones of purely quartz adjacent to areas of quartz grains with carbonate cement suggest partial silicification (XPL); crosscutting carbonate veins present; (D) DEH JAS 018.2 – opaque anhedral disseminated Fe-oxide aggregates appear black or dark brown (PPL); sample is partially silicified as indicated by remnant limestone sections with calcite veining; (E) DEH JAS 018.2 – partially silicified sample; remnant limestone sections with dark brown rhombs of Fe-oxide, possibly goethite replacing dolomite or rhombic goethite (PPL); (F) DEH JAS 008 – partially silicified sample; 70% of mineralogy is recrystallized jigsaw quartz; carbonate protolith with fossil sponge and crinoid bioclasts that remain reactive to 10% HCl; Fe-oxide staining and disseminated dark brown Fe-oxide aggregates measuring up to 500 μm occur throughout (PPL).

and aluminum (0.82). The rare earth elements generally show strong to moderate correlations with aluminum and potassium. Iron and magnesium are negatively correlated, likely due to the fact that they commonly substitute for one another in the carbonate protoliths and in the abundant oxide minerals. We consider P_2O_5 as a proxy for apatite, as apatite is the only phosphate-bearing mineral that we identify in our samples. There is a moderate negative correlation between SiO_2 and P_2O_5, suggesting that more intensely silicified rocks have less apatite.

5.3. Fe-oxide (U-Th)/He dating

5.3.1. Sample aliquot grain characterization

Hand separated, microdrilled, crushed, and disaggregated (EPD) jasperoid aliquots selected for (U-Th)/He

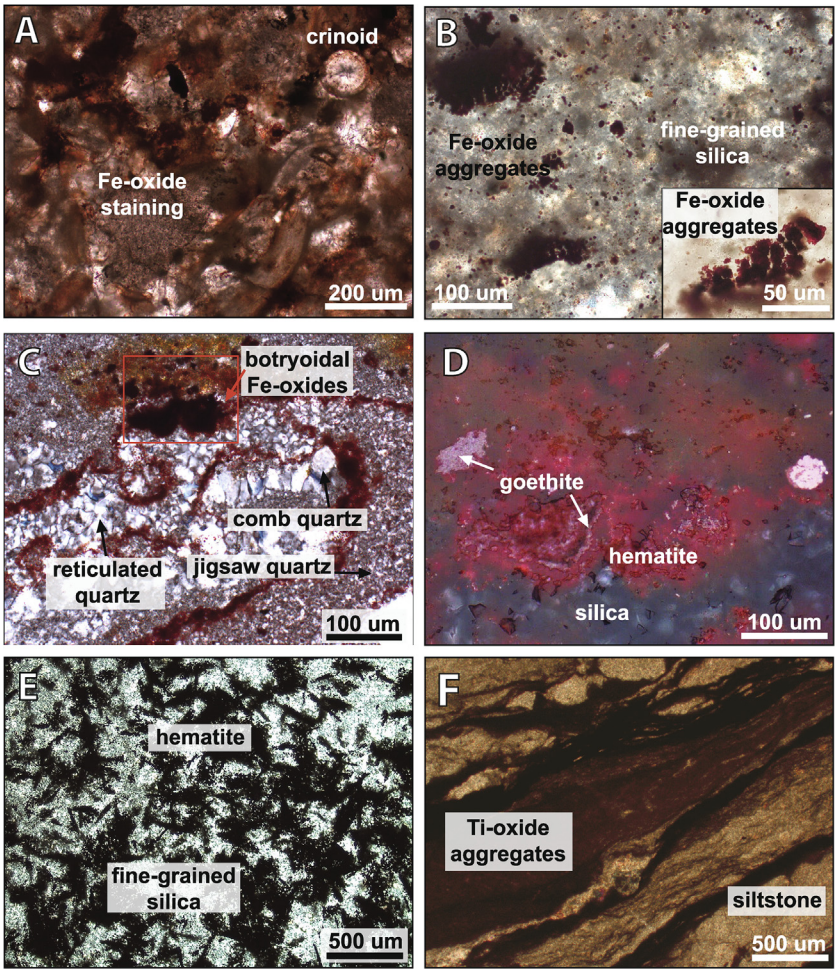

Fig. 6. Photomicrographs of silica and Fe-oxide textures from Battle Mountain and Gold Quarry samples: (A) DEH JAS 009 – heavily Fe-oxide stained siltstone with remnant carbonate fossil and crinoid bioclasts (PPL); (B) DEH JAS 011 – siltstone with disseminated dark red Fe-oxides and large aggregates measuring up to 200 μm composed of anhedral plates in a pseudo-dendritic pattern (PPL); (C) DEH JAS 012 – strongly silicified jasperoid with a jigsaw quartz matrix, reticulated quartz, and comb quartz veins (XPL); Fe-oxides rim quartz veins and are disseminated throughout sample in 25 μm ellipsoids; two botryoidal Fe-oxide aggregates more than 100 μm wide occur in the area outlined in red; (D) DEH JAS 012 – field of view indicated by red box in previous image; reflected light (RFL) reveals botryoidal dark red hematite with internal reflectance and silvery grey goethite; (E) DEH JAS 014 – jigsaw quartz with elongated and crosscutting opaque black hematite aggregates in a pattern that resembles snowflake obsidian (XPL); (F) DEH JAS 015 – siltstone with translucent to opaque maroon oxide veinlets that contain siltstone clasts (PPL); none of the veinlets were visible in BSE images and the only oxide minerals identified during EDX spot analysis were micron to submicron Ti-oxides. (For interpretation of the references to color in this figure legend, the reader is referred to the web version of this article.)

dating consist of silicified rock with Fe-oxide patches measuring ten to hundreds of microns on the grain surface (Fig. 10B). The range of crystal dimensions and corresponding closure temperatures for each Fe-oxide morphology and jasperoid sample are listed in Table 3. The Fe-oxides display blocky (Fig. 10C), platelet, and acicular crystal morphologies. The disaggregated samples are more concentrated and predominantly comprise Fe-oxides with 25 μm patches of silica and barite (Fig. 10D). We observe a distinctive pitted texture (Fig. 10E) and radiating acicular goethite (Fig. 10F) in disaggregated grains.

5.3.2. Fe-oxide (U-Th)/He dates

We dated a total of 28 aliquots from eight samples using (U-Th)/He chronology. The dates range from 29.4 ± 0.5 Ma to 0.11 ± 0.01 Ma (Table 4). Fig. 11 compares He dates among all samples. The two Gold Quarry samples show intersample variation, despite coming from the same outcrop: aliquots from DEH JAS 011 are from a goethite surface rind, whereas aliquots from DEH JAS 012 are disseminated aggregates of acicular goethite.

Marigold samples generally yield the oldest dates. Fe-oxides separated using two different techniques from DEH JAS 006 yield non-contemporaneous He dates. The

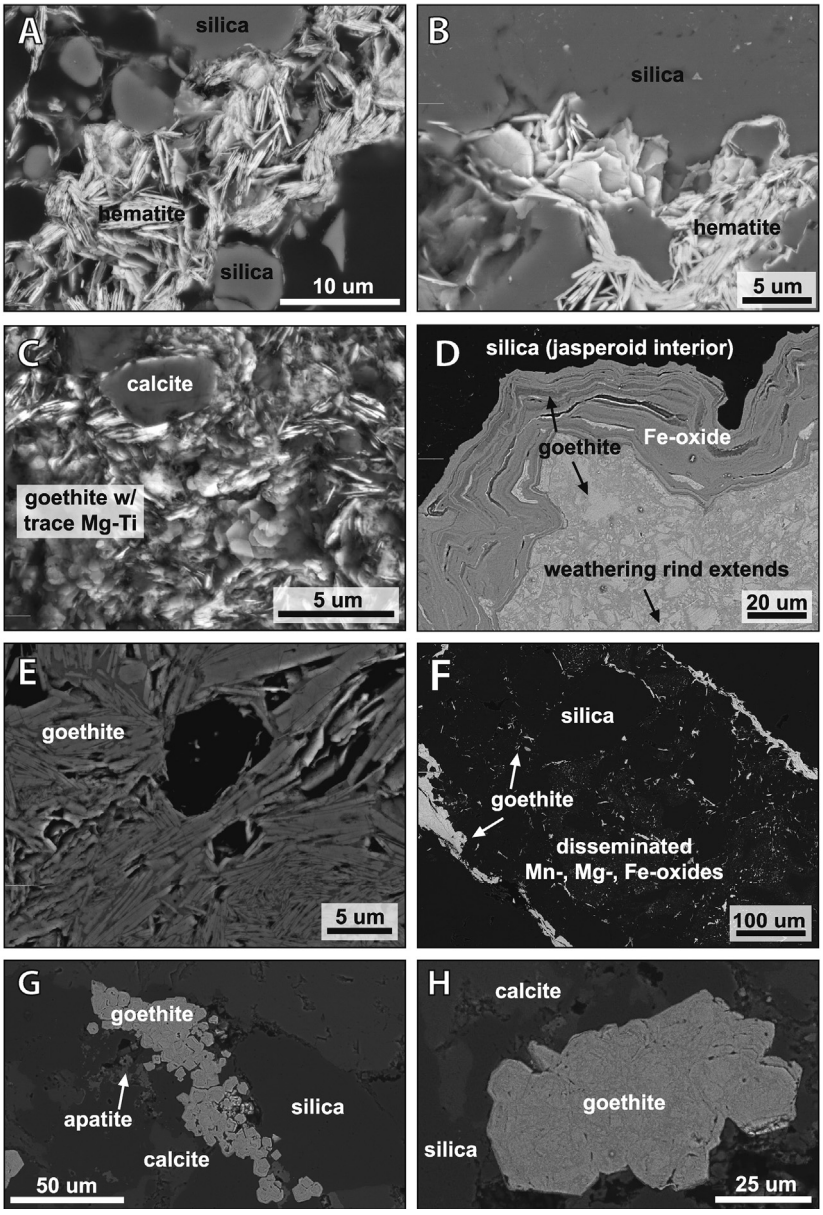

Fig. 7. Back-scattered electron images of Fe-oxides from Marigold samples: (A) DEH JAS 002 – hematite platelets; where imaged perpendicular to c-axis, the platelets appear acicular; (B) DEH JAS 002 – hematite platelets showing roughly hexagonal morphology; (C) DEH JAS 004 – dense aggregate of hexagonal goethite platelets; trace Mg and Ti in goethite identified by EDX spot analysis; (D) DEH JAS 004 – jasperoid interior is silica; surficial weathering rind show colliform goethite bands with fluctuating composition across the rind; outermost layer is goethite with an internally brecciated texture; (E) DEH JAS 006 – aggregate of shreddy goethite laths; (F) DEH JAS 006 – Shreddy and acicular goethite crystals rimming what appeared to be an oxide veinlet in optical petrography, but is predominantly silica in BSE imagery; micron-scale rounded to anhedral Mn-, Mg-, and Fe-oxides are spaced less than 10 μm apart in veinlet interior; (G) DEH JAS 018 – individual zoned cubic to pentagonal goethite crystals 5 μm wide cluster to form an aggregate 100 μm long; trace apatite observed adjacent to goethite aggregate; (H) DEH JAS 018 – goethite aggregate where individual crystals are difficult to distinguish, although internal zonation suggests they were roughly hexagonal; internal texture is brecciated.

(U-Th)/He analyses performed on disaggregated Fe-oxides produce highly reproducible dates within the Pliocene (4.25 ± 0.06 Ma, 4.24 ± 0.06 Ma, 4.09 ± 0.07 Ma, 5.76 ± 0.08 Ma). By contrast, the hand separated Fe-oxide aliquots yield Late Pleistocene dates (0.14 ± 0.01 to 0.11 ± 0.01 Ma), with the exception of one grain at 7.36 ± 0.10 Ma.

The He dates from Battle Mountain samples range from 29.4 ± 0.5 Ma to 0.97 ± 0.07 Ma. We lost Nb-tubes from samples DEH JAS 008 and DEH JAS 009 while preparing aliquots for U-Th analysis following He degassing, so we can only report the He dates from the two dated aliquots for each sample. The data are insufficient to make interpretations about these samples, so we will

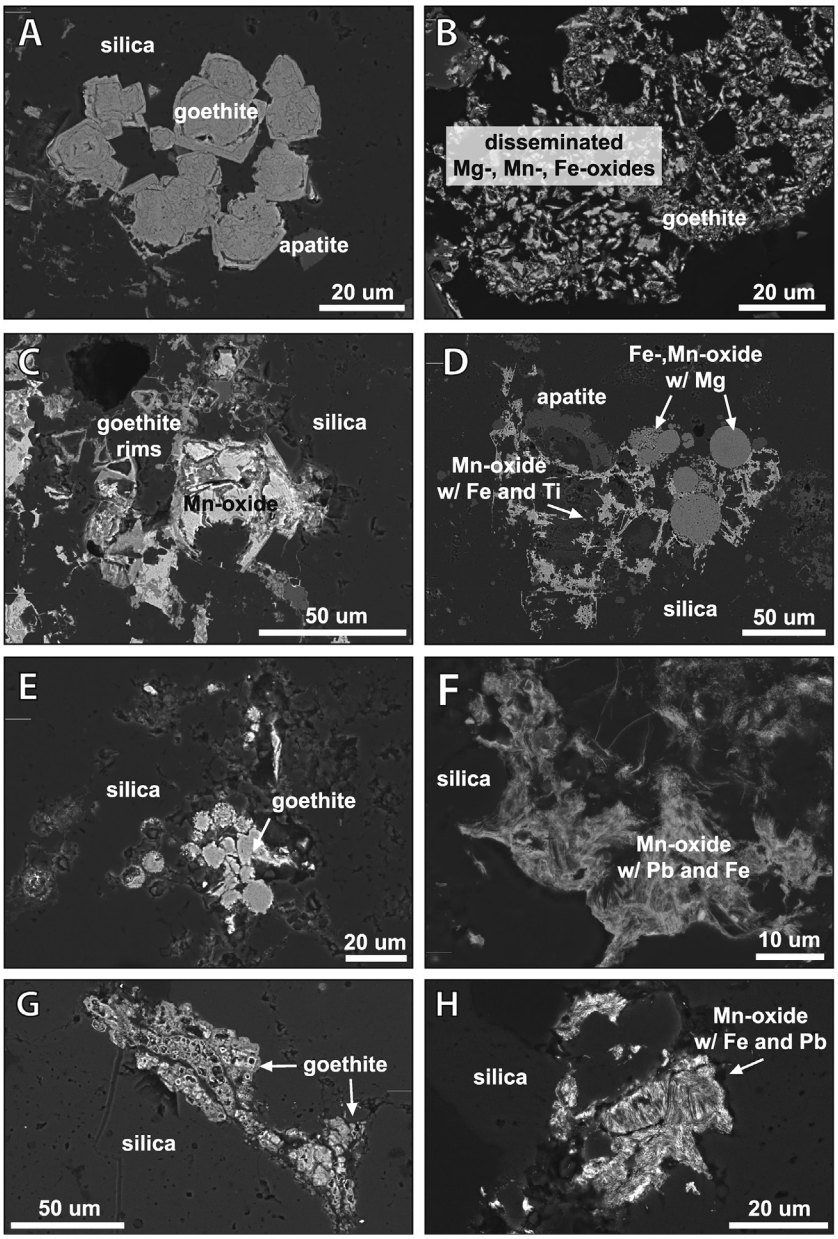

Fig. 8. Back-scattered electron images of Fe-oxides from Marigold and Battle Mountain samples: (A) DEH JAS 018.2 – irregularly zoned rounded goethite cores with cubic to pentagonal rims; (B) DEH JAS 018.2 – shreddy goethite surrounded by submicron granular to acicular Mg-, Mn-, and Fe-oxides; (C) DEH JAS 018.2 – shreddy Mn-oxide with goethite rims and fracture fill; (D) DEH JAS 018.2 – spherical aggregates composed of 1 μm Fe- and Mn-oxide spheres intergrown with apatite and shreddy skeletal Mn-oxide; (E) DEH JAS 008 – subhedral to spherical goethite nodules with framboidal rims; (F) DEH JAS 008 – feathery to acicular submicron Mn-oxide aggregates; (G) DEH JAS 009 – possible goethite fossil replacement or void fill; polygonal porosity outlined with a brighter mineral in BSE that could not be distinguished from goethite with EDX spot analysis; (H) DEH JAS 009 – stacked "books" of Mn-oxide sheets.

not focus on DEH JAS 008 or DEH JAS 009 in the discussion.

5.3.3. Calculated Fe-oxide closure temperatures

Taken together, the full range of effective closure temperatures as a function of grain size is 26–136 °C (Table 3). The only hematite grains for which closure temperature was calculated are the hematite platelets in sample DEH JAS 002; all other closure temperatures were calculated for goethite morphologies. The hematite platelets have the highest calculated closure temperature (136 °C), reflecting the differences in the diffusion kinetics between hematite and goethite. For goethite, platelet morphologies have the lowest calculated closure temperatures, whereas bladed morphologies have the highest closure temperatures (Table 3). Grain size rather than morphology appears to dictate the closure temperature values for anhedral, granular, spherical, and bladed morphologies (Table 3). The closure temperatures for crystals

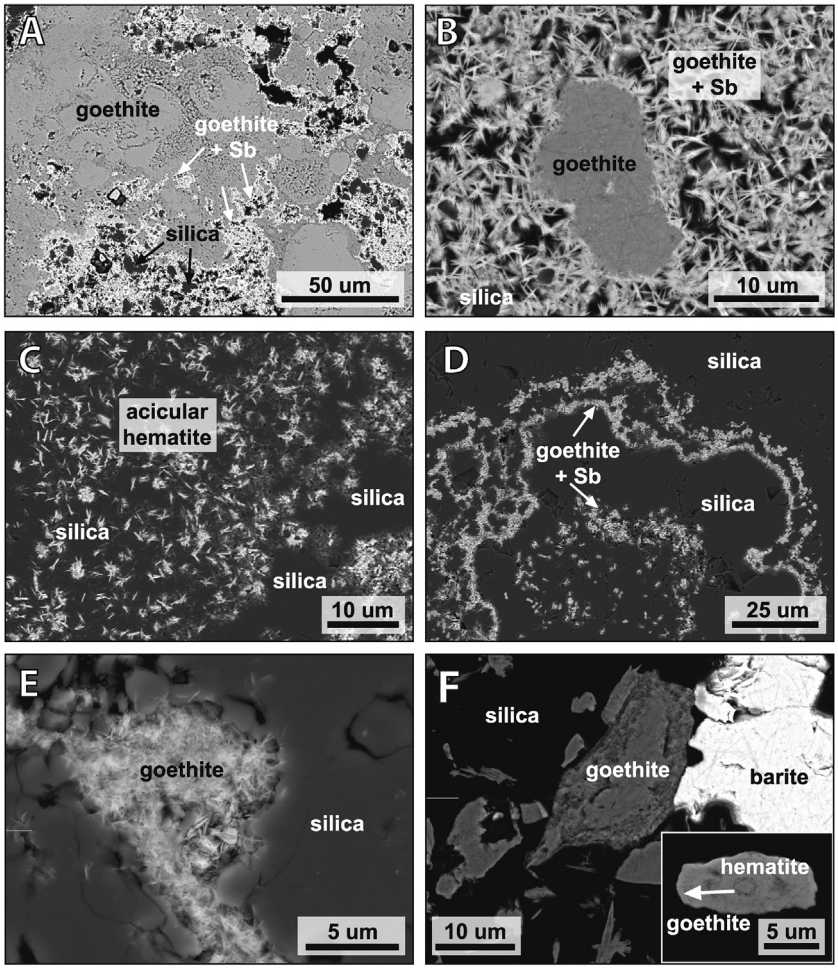

Fig. 9. Back-scattered electron images of Fe-oxides from Gold Quarry samples: (A) DEH JAS 011 – massive goethite rim with rounded internal sections surround by massive, pitted goethite; acicular goethite crystals 2 μm long line void spaces in the rim; EDX spot analysis identified Sb within the acicular goethite zones; (B) DEH JAS 011 – magnified view of acicular goethite where EDX also detects Sb; (C) DEH JAS 012 – disseminated acicular hematite; (D) DEH JAS 012 – acicular goethite rimming botryoidal colliform silica; (E) DEH JAS 013 – submicron acicular goethite; (F) DEH JAS 014 – shreddy acicular and tabular goethite crystals; crystals coarser than 20 μm show pitted dissolution zones; where chemical zonation is visible, Fe-oxides show a hematite core zoning outwards to a goethite rim.

with acicular morphologies are high considering the grain dimensions are commonly submicron, ranging from 67–101 °C (Table 3). These elevated closure temperatures reflect the length-scale control on He diffusion domain (Meesters and Dunai, 2002).

6. DISCUSSION

Certain physical characteristics of Fe-oxides show a promising association with Au content in jasperoid samples, which we discuss in Section 6.1. In this section, we also evaluate the whole-rock geochemistry results and how they relate to jasperoid prospectivity in the context of findings from previous studies. The Fe-oxide He date results show a wide range, and we discuss the possible causes of the observed date variation in Section 6.2.

6.1. Jasperoid prospectivity and Fe-oxide characteristics

Although many authors have attempted to distinguish different jasperoid generations with the goal of identifying those contemporaneous with Au mineralization (Lovering, 1972; Holland et al., 1988; Nelson, 1990; Theodore and Jones, 1991; Hofstra, 1994; Emsbo, 1999; Yigit et al., 2006), until now no studies have examined whether Au-bearing jasperoids display unique Fe-oxide features. In Section 6.1.1, we highlight how our textural observations on Fe-oxides could be used to assess jasperoid prospectivity. In Section 6.1.2, we integrate our limited whole-rock geochemical dataset with the results of previous studies to evaluate the element suite related to Au mineralization. We incorporate our prospective Fe-oxide characteristics and geochemistry results with the silica

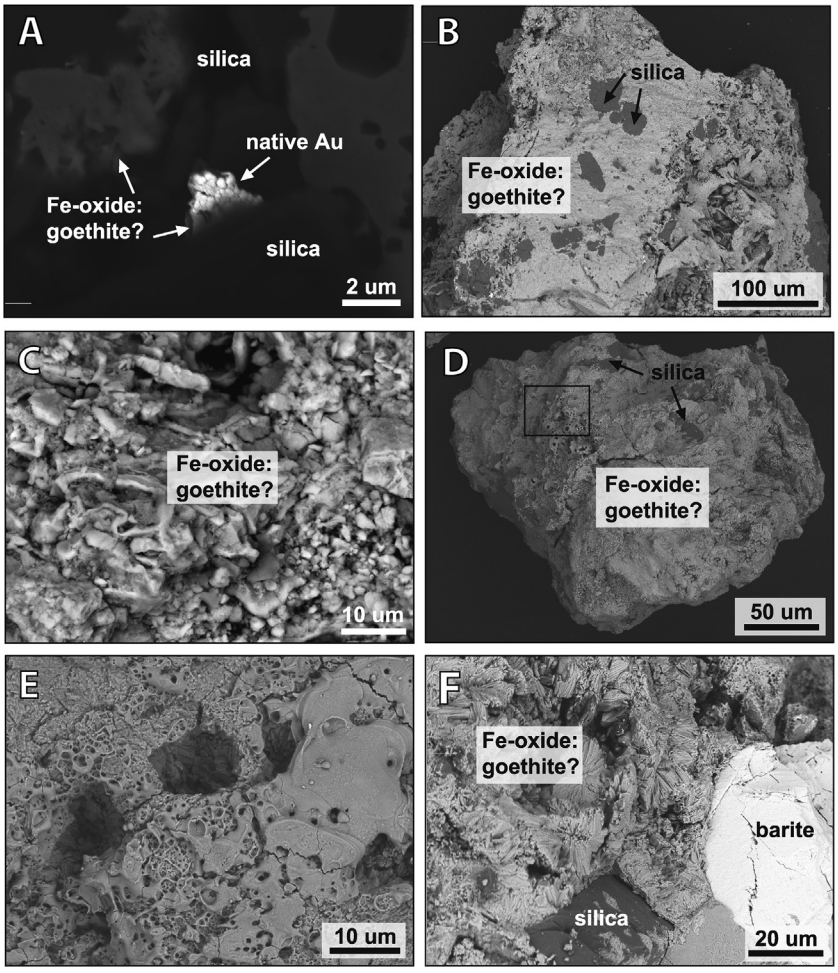

Fig. 10. Gold deportment and Fe-oxide (U-Th)/He sample aliquot characterization: (A) DEH JAS 014 – shreddy to acicular Fe-oxide surrounding and adjacent to native Au detected during a bright phase search; gold occurs as a thin botryoidal aggregate, measuring 2 μm in length; (B) DEH JAS 006 – hand separated grain from Marigold duplicate sample; grain surface shows 5% silica patches, remainder of grain surface is Fe-oxide and voids between bladed morphologies, possibly from dissolution; individual Fe-oxide crystals appear as fine flakes; (C) DEH JAS 010 – blocky and polygonal Fe-oxides from a Battle Mountain sample; EDX spectra were inconclusive for mineral identification; (D) DEH JAS 006 – disaggregated grain from Marigold duplicate sample; grain surface shows 5% silica patches and the Fe-oxides have a distinctive pitted texture; black box indicates field of view for subsequent image; (E) DEH JAS 006 – magnified view of pitted texture on grain surface of disaggregated duplicate sample from Marigold; (F) DEH JAS 006 – radiating acicular Fe-oxide (goethite?) in cross-section on the surface of a disaggregated grain from Marigold duplicate sample; trace barite in grain.

characteristics, indicator element signatures, and mineralogy results from previous authors in Table 5 to summarize jasperoid prospectivity criteria for future exploration programs.

6.1.1. Textural prospectivity indicators

Although using whole-rock geochemistry to identify potential deposits is standard practice in mineral exploration, we propose that optical petrography and SEM may be simpler and more cost-effective methods when evaluating jasperoids as an indicator of prospectivity. We acknowledge that our sample size is small; however, within our sample set, optical petrography and SEM definitively reveal Fe-oxide crystal morphologies and textures specific to mineralized jasperoids.

The most diagnostic feature of mineralized samples (Fig. 9) is the abundance of extremely fine-grained (<100 nm wide) feathery to acicular Fe-oxides (Fig. 9E). Additional Fe-oxide textures observed only in mineralized samples include concentric zonation from hematite to goethite (Fig. 9F) and botryoidal textures (Figs. 6C, D and 9A, D). The latter texture appears to represent Fe-oxides coating colloform silica with a botryoidal surface (Fig. 9D), rather than botryoidal crystal form of the Fe-oxides themselves. Colloform silica may represent recrystallization of amorphous silica gel, providing insight into the conditions of jasperoid silicification (Fournier, 1985; Saunders, 1994; Taksavasu et al., 2018). In contrast to the mineralized samples, zonation in unmineralized samples occurs as weathering rinds (Fig. 7D), concentric zonation

Table 2
A select array of trace element Spearman correlation coefficients[1] for 18 jasperoid samples from Gold Quarry, Marigold, and Battle Mountain locations.

	Au	As	Sb	Hg	SiO_2	Fe_2O_3(T)	MnO	MgO	CaO	P_2O_5	V	Co	Ni	Zn	Cu	Ag	Pb	Ga	Mo	Sn	Ba	W	Tl	Bi	U
Au	**1**	**0.78**	0.79	0.02	-0.15	-0.16	-0.28	0.26	0.10	0.05	0.49	-0.07	-0.02	0.40	0.45	**0.66**	**0.85**	0.42	0.24	0.45	0.29	**0.79**	**0.88**	0.27	**0.78**
As	**0.78**	**1**	**0.94**	0.17	-0.29	0.22	-0.35	-0.14	-0.18	0.18	**0.52**	0.02	0.08	0.33	**0.56**	**0.63**	**0.86**	0.28	0.48	**0.65**	0.34	**0.72**	**0.78**	**0.51**	**0.69**
Sb	**0.79**	**0.94**	**1**	0.14	-0.19	0.05	-0.34	0.01	-0.13	0.20	**0.56**	0.01	0.06	0.42	**0.58**	**0.73**	**0.83**	0.40	0.47	**0.55**	0.28	**0.84**	**0.81**	0.37	**0.72**
Hg	0.02	0.17	0.14	**1**	0.18	-0.05	0.33	-0.26	-0.17	-0.19	0.21	0.01	-0.11	0.38	-0.01	0.13	-0.04	-0.12	-0.30	0.04	0.14	0.06	-0.38	0.06	0.41
SiO_2	-0.15	-0.29	-0.19	0.18	**1**	0.12	-0.02	-0.18	-0.33	**-0.52**	0.09	0.21	0.06	-0.21	0.20	0.00	-0.25	0.24	0.35	-0.14	0.15	0.00	0.11	-0.08	-0.29
Fe_2O_3(T)	-0.16	0.22	0.05	-0.05	0.12	**1**	-0.23	**-0.69**	**-0.84**	-0.25	0.39	0.31	**0.55**	0.33	0.25	-0.27	0.07	-0.11	**0.70**	0.46	0.33	0.05	0.05	0.41	-0.34
MnO	-0.28	-0.35	-0.34	0.33	-0.02	-0.23	**1**	-0.20	0.33	0.09	-0.36	-0.11	-0.17	0.09	**-0.53**	-0.05	-0.21	-0.45	-0.38	-0.41	-0.48	-0.41	**-0.57**	-0.42	-0.28
MgO	0.26	-0.14	0.01	-0.26	-0.18	**-0.69**	-0.20	**1**	**0.60**	0.11	-0.15	0.12	-0.14	0.42	0.16	0.07	-0.05	0.47	**-0.60**	-0.27	0.15	0.18	0.11	-0.37	0.32
CaO	0.10	-0.18	-0.13	-0.17	-0.33	**-0.84**	0.33	**0.60**	**1**	0.30	**-0.58**	-0.20	**-0.55**	0.38	-0.22	0.18	-0.05	0.10	**-0.70**	-0.31	-0.17	-0.20	-0.20	-0.39	0.25
P_2O_5	0.05	0.18	0.20	-0.19	**-0.52**	-0.25	0.09	0.11	0.30	**1**	0.10	-0.13	0.30	**0.61**	-0.13	0.09	-0.13	0.10	-0.22	-0.33	-0.16	-0.08	-0.10	-0.39	0.32
V	0.49	**0.52**	**0.86**	0.21	0.09	0.39	-0.36	-0.15	-0.58	0.10	**1**	0.20	**0.62**	0.32	0.42	0.21	0.39	0.45	0.38	0.16	0.22	**0.56**	**0.63**	-0.01	0.41
Co	-0.07	0.02	0.01	0.01	0.21	0.31	-0.11	0.12	-0.20	-0.13	0.20	**1**	**0.50**	0.12	0.49	-0.10	-0.04	0.34	0.04	-0.04	0.36	0.07	0.00	-0.27	-0.24
Ni	-0.02	0.08	0.06	-0.11	0.06	**0.85**	-0.17	-0.14	**-0.55**	0.30	**0.62**	**0.50**	**1**	0.27	0.24	-0.34	-0.15	0.31	0.35	-0.12	0.20	0.08	0.06	-0.35	-0.17
Zn	0.40	0.33	0.42	0.38	-0.21	-0.33	0.09	0.42	0.38	**0.61**	0.32	0.12	0.27	**1**	0.26	0.23	0.10	**0.58**	-0.18	-0.14	0.31	0.34	0.27	-0.40	**0.51**
Cu	0.45	**0.56**	**0.58**	-0.01	0.20	0.25	**-0.53**	0.16	-0.22	-0.13	0.42	0.49	0.24	0.26	**1**	0.23	0.45	**0.73**	0.41	0.40	**0.67**	**0.55**	**0.56**	0.24	0.44
Ag	**0.66**	**0.63**	**0.73**	0.13	0.00	-0.27	-0.05	0.07	0.18	0.09	0.21	-0.10	-0.34	0.39	0.23	**1**	**0.59**	0.18	0.22	0.33	0.24	**0.69**	**0.64**	0.30	**0.60**
Pb	**0.85**	**0.86**	**0.83**	-0.04	-0.25	0.07	-0.21	-0.05	-0.05	-0.13	0.39	-0.04	-0.15	0.10	0.45	**0.59**	**1**	0.16	0.38	**0.68**	0.18	**0.74**	**0.75**	**0.51**	**0.63**
Ga	0.42	0.28	0.40	-0.12	0.24	-0.11	-0.45	0.47	-0.01	0.10	0.45	0.34	0.31	**0.58**	**0.73**	0.18	0.16	**1**	0.09	-0.01	0.47	**0.54**	0.49	-0.17	0.40
Mo	0.24	0.48	0.47	-0.30	0.35	**0.70**	-0.38	**-0.60**	**-0.70**	-0.22	**0.53**	0.04	0.35	-0.18	0.41	0.22	0.38	0.09	**1**	**0.57**	0.33	0.45	**0.50**	0.46	0.04
Sn	0.45	**0.65**	**0.55**	0.04	-0.14	0.46	-0.41	-0.27	-0.31	-0.33	0.16	-0.04	-0.12	-0.14	0.40	0.33	**0.68**	-0.01	**0.57**	**1**	**0.55**	**0.54**	**0.55**	**0.84**	0.25
Ba	0.29	0.34	0.28	0.14	0.15	0.33	-0.48	0.15	-0.17	-0.16	0.22	0.36	0.20	0.31	**0.67**	0.24	0.18	0.47	0.33	**0.55**	**1**	0.43	0.41	0.38	0.25
W	**0.79**	**0.72**	**0.84**	0.06	0.00	0.05	-0.41	0.18	-0.20	-0.08	**0.56**	0.07	0.08	0.34	**0.55**	**0.69**	**0.74**	**0.54**	0.45	**0.54**	0.43	**1**	**0.82**	0.36	**0.55**
Tl	**0.88**	**0.78**	**0.81**	-0.38	0.11	0.05	**-0.57**	0.11	-0.20	-0.10	**0.63**	0.00	0.06	0.27	**0.56**	**0.64**	**0.75**	0.49	**0.50**	**0.55**	0.41	**0.82**	**1**	0.41	**0.68**
Bi	0.27	**0.51**	0.37	0.06	-0.08	0.41	-0.42	-0.37	-0.37	-0.39	-0.01	-0.27	-0.35	-0.40	0.24	0.30	**0.51**	-0.17	0.46	**0.84**	0.38	0.36	0.41	**1**	0.20
U	**0.78**	**0.69**	**0.72**	0.41	-0.29	-0.34	-0.28	0.32	0.25	0.32	0.41	-0.24	-0.17	**0.51**	0.44	**0.60**	**0.63**	0.40	0.04	0.25	0.25	**0.55**	**0.68**	0.20	**1**

All correlations >0.5 are bold; light-gray shading indicates correlations greater than 0.5 but less than 0.75; dark-gray shading indicates correlations greater than or equal to 0.75; black boxes indicate like-to-like correlations of 1 and are omitted. We consider coefficients between 0.25 and 0.5 as weak, coefficients between 0.5 and 0.75 as moderate, and coefficients between 0.75 and 1 as strong.

in goethite (Figs. 7G; 8A), and irregular, patchy, "brecciated" zonation (Figs. 7D, H; 8A). Fe-oxides in unmineralized samples display a range of crystal morphologies including: plates, blades, granular, and cubic pseudomorphs after pyrite (Figs. 7, 8). These pseudomorphs may represent oxidation of relatively coarse diagenetic pyrite in unmineralized protoliths, whereas our mineralized samples would have lacked this pyrite style and likely originally contained the fine-grained, disseminated sulfides typical of CTGD Au mineralization (Hofstra and Cline, 2000; Cline et al., 2005).

In order to use Fe-oxide characteristics to identify prospective jasperoids, we recommend that future studies should collect multiple samples and prepare multiple thin sections per outcrop, as Au concentration, Fe-oxide mineralogy, and Fe-oxide crystal morphology vary among our study areas and also within our study areas at the outcrop scale (Table 1). Although mineralized jasperoids display unique Fe-oxide characteristics in our sample set, future research must assess if these observations are consistent across additional study sites in Nevada and elsewhere.

6.1.2. Geochemical prospectivity indicators

In addition to correlating our identified Fe-oxide characteristics with Au content of the samples, we analyzed our whole-rock geochemistry results to see if they would produce an indicator element suite that agreed with published exploration studies of jasperoids (Lovering, 1972; Holland et al., 1988; Nelson, 1990; Theodore and Jones, 1991; Hofstra, 1994; Emsbo, 1999; Yigit et al., 2006). Our Spearman correlation table indicates that the elements that positively correlate with Au in our dataset are: As, Ag, Pb, Sb, Tl, U, and W (Table 2). We acknowledge that our sample size is small; however, the near identical match between our indicator element suite and that of Holland et al. (1988; 65 samples from 10 CTGDs and 22 barren systems; Table 5) suggests that our statistical analysis is robust enough to interpret general trends and their significance to jasperoid prospectivity. Our indicator element suite also aligns with the other published studies, albeit differing to some degree where those studies included jasperoids from other deposit types (Lovering, 1972; Theodore and Jones, 1991), or due to subtle differences in characteristics of the individual deposits analyzed. For example, Yigit et al. (2006) identified Hg as an indicator element in the Gold Bar district, whereas Hg is not associated with Au in our samples. The Au deposits in the Gold Bar district formed at shallower depths than at Gold Quarry (Cline et al., 2005), and higher Hg concentrations are commonly associated with shallow Au mineralization (Goldfarb et al., 2016). Our element signature contrasts to some extent with the discriminant function of Nelson (1990), likely because he elected to use Q-mode factor analysis which identified rock composition end members rather than elemental associations. Nelson (1990) also generated a discriminant function that successfully categorized 95% of mineralized samples when applied to new data. However, the function struggled to classify unmineralized samples, produced false positives, and required recalibration for new datasets. We suggest that Fe-oxide textures

Table 3
Calculated closure temperatures for observed jasperoid Fe-oxide morphologies.

Fe-Oxide Sample and Morphology	a[a] (μm) mean	a (μm) max	a (μm) min	a SD (μm)	T_c[b] (°C) mean	T_c (°C) max	T_c (°C) min	Geometry	Reference used
DEH JAS 002 hematite platelet	0.086	0.223	0.032	0.041	119	136	106	Plane sheet	Farley and Flowers (2012) Evenson et al. (2014)
DEH JAS 004 individual goethite rim zone	0.453	1.096	0.171	0.261	76	88	67	Plane sheet	Shuster et al. (2005)
DEH JAS 004 goethite platelet	0.042	0.064	0.028	0.011	32	37	28	Plane sheet	Reiners et al. (2014)
DEH JAS 006 bladed goethite	0.158	0.698	0.036	0.112	97	121	79	Cylinder	Garcia et al. (2017)
DEH JAS 006 granular goethite	1.251	8.448	0.243	1.690	55	88	42	Sphere	Reiners et al. (2014)
DEH JAS 008 acicular goethite in aggregate	0.108	0.162	0.059	0.027	94	99	86	Cylinder	Garcia et al. (2017)
DEH JAS 008 spherical goethite aggregate	3.671	5.388	2.506	0.740	75	81	70	Sphere	Reiners et al. (2014)
DEH JAS 009 blocky goethite in aggregate	0.541	1.900	0.160	0.312	50	67	37	Sphere	Reiners et al. (2014)
DEH JAS 010 goethite aggregate	0.492	1.476	0.213	0.259	60	76	51	Plane sheet	Reiners et al. (2014)
DEH JAS 011 acicular goethite in rim	0.080	0.184	0.029	0.027	89	101	77	Cylinder	Garcia et al. (2017)
DEH JAS 011 botryoidal goethite rim aggregate	8.179	17.264	2.843	5.128	98	110	88	Sphere	Shuster et al. (2005)
DEH JAS 011 disseminated acicular goethite	0.054	0.097	0.035	0.013	84	92	79	Cylinder	Garcia et al. (2017)
DEH JAS 012 acicular goethite	0.076	0.146	0.026	0.028	88	98	75	Cylinder	Garcia et al. (2017)
DEH JAS 013 acicular goethite	0.035	0.081	0.013	0.012	79	90	67	Cylinder	Garcia et al. (2017)
DEH JAS 014 anhedral zoned goethite	2.146	6.687	0.060	1.570	63	84	26	Sphere	Reiners et al. (2014)
DEH JAS 018 goethite aggregate	2.465	18.056	0.220	4.889	57	99	40	Sphere	Reiners et al. (2014)
DEH JAS 018 individual zoned goethite	3.556	10.505	1.945	2.128	74	91	67	Sphere	Reiners et al. (2014)
DEH JAS 018–2 individual zoned goethite	5.851	11.491	2.217	2.648	81	92	69	Sphere	Reiners et al. (2014)
DEH JAS 018–2 spherical goethite aggregate	9.865	17.974	3.987	5.315	88	99	77	Sphere	Reiners et al. (2014)
DEH JAS 018–2 spherical individual goethite	0.339	0.566	0.142	0.113	45	51	36	Sphere	Reiners et al. (2014)

[a] Diffusion domain length-scale is plate half-width or crystal radius measured from SEM SE images.
[b] Closure temperatures calculated assuming spherical geometry, 10 °C/Myr cooling rate, and the diffusion kinetics (E_a and D_0) from Farley and Flowers (2012), Evenson et al. (2014); Shuster et al. (2005), Reiners et al. (2014), and Garcia et al. (2017) depending on the Fe-oxide mineralogy and crystal morphology.

Table 4
(U-Th)/He results from jasperoid Fe-oxide aliquots from Marigold, Battle Mountain, and Gold Quarry.

Site	Sample Name	Aliquot Length (μm)	Aliquot Width (μm)	Fe-oxide Separation Method	Measured He Age (Ma)	± (1σ)	He (pmol)	± (1σ)	U (ng)	± (1σ)	Th (ng)	± (1σ)	Fe-oxide Aliquot[1] Mass (mg)	U (ppm)	Th (ppm)	eU (U + 0.235 Th)
Marigold	DEH JAS 004_1	—	—	Microdrilled	7.41	0.12	0.0103	0.000112	0.2350	0.0034	0.1008	0.0015		—	—	—
	DEH JAS 004_2	480	306		11.9	0.2	0.0022	3.098E−05	0.0293	0.0004	0.0186	0.0003	0.101	0.289	0.184	0.332
	DEH JAS 004_3	370	273		10.2	0.2	0.0038	4.608E−05	0.0621	0.0009	0.0256	0.0004	0.062	0.997	0.412	1.094
	DEH JAS 004_4	484	334		9.33	0.17	0.0075	9.411E−05	0.1434	0.0021	0.0272	0.0004	0.122	1.176	0.223	1.229
	DEH JAS 004_5	576	320		5.73	0.42	0.0002	1.124E−05	0.0042	0.0001	0.0039	0.0001	0.133	0.032	0.029	0.039
	DEH JAS 006_HS_1	267	224	Hand separated	0.135	0.003	0.0005	9.93E−06	0.5193	0.0074	0.5095	0.0073	0.030	17.194	16.867	21.157
	DEH JAS 006_HS_2	313	304		0.119	0.002	0.0010	1.118E−05	1.2211	0.0176	1.3352	0.0192	0.065	18.830	20.589	23.668
	DEH JAS 006_HS_3	367	260		0.109	0.002	0.0009	7.454E−06	1.2483	0.0181	1.1840	0.0180	0.056	22.373	21.219	27.360
	DEH JAS 006_HS_4	409	380		7.36	0.10	0.0150	4.267E−05	0.3557	0.0051	0.0958	0.0014	0.133	2.676	0.721	2.845
	DEH JAS 006_LS_1	255	239	EPD and Frantz	4.25	0.06	0.0056	2.443E−05	0.2345	0.0034	0.0408	0.0006	0.033	7.146	1.244	7.438
	DEH JAS 006_LS_2	444	374		4.24	0.06	0.0084	5.15E−05	0.3644	0.0053	0.0232	0.0004	0.140	2.604	0.166	2.642
	DEH JAS 006_LS_3	346	192		4.09	0.07	0.0061	1.632E−05	0.2703	0.0051	0.0255	0.0006	0.029	9.472	0.892	9.681
	DEH JAS 006_LS_4	305	289		5.76	0.08	0.0090	2.834E−05	0.2869	0.0041	0.0193	0.0003	0.057	5.028	0.338	5.108
Battle Mountain	DEH JAS 008_1	283	194	Crushed and Frantz	2.37	0.13	0.0005	2.655E−05	0.0374	0.0005	0.0081	0.0002	0.024	1.562	0.339	1.642
	DEH JAS 008_3	258	157		1.61	0.12	0.0003	2.156E−05	0.0317	0.0005	0.0053	0.0001	0.0142	2.223	0.371	2.310
	DEH JAS 009_1	154	116		1.14	0.28	0.0001	2.431E−05	0.0143	0.0002	0.0081	0.0002	0.0047	3.058	1.739	3.466
	DEH JAS 009_2	145	118		3.16	0.97	0.0001	3.728E−05	0.0061	0.0001	0.0045	0.0001	0.0045	1.346	1.002	1.581
	DEH JAS 010_1	145	125	Crushed and Frantz	6.20	0.13	0.0022	3.397E−05	0.0649	0.0009	0.0054	0.0001	0.0051	12.650	1.053	12.897
	DEH JAS 010_2	131	71		0.97	0.07	0.0002	1.381E−05	0.0340	0.0005	0.0136	0.0003	0.0015	22.629	9.055	24.757
	DEH JAS 010_3	153	102		29.4	0.5	0.0044	4.59E−05	0.0196	0.0003	0.0343	0.0005	0.0036	5.478	9.584	7.730
Gold Quarry	DEH JAS 011_1	509	398	Microdrilled	1.19	0.03	0.0004	7.159E−06	0.0430	0.0007	0.0791	0.0012	0.181	0.238	0.437	0.340
	DEH JAS 011_2	498	384		2.68	0.03	0.0028	1.475E−05	0.1663	0.0024	0.1296	0.0019	0.165	1.006	0.784	1.190
	DEH JAS 011_3	385	311		3.16	0.04	0.0017	1.242E−05	0.0794	0.0012	0.0802	0.0012	0.084	0.951	0.960	1.176
	DEH JAS 011_4	308	297		2.07	0.04	0.0021	3.008E−05	0.1517	0.0022	0.1461	0.0021	0.061	2.474	2.384	3.034
	DEH JAS 012_1	378	256	Microdrilled	0.43	0.02	0.0001	3.976E−06	0.0365	0.0007	0.0625	0.0012	0.056	0.656	1.125	0.921
	DEH JAS 012_2	374	254		0.46	0.02	0.0001	4.997E−06	0.0360	0.0006	0.0688	0.0011	0.054	0.664	1.271	0.963
	DEH JAS 012_3	197	126		0.38	0.04	0.0000	4.263E−06	0.0134	0.0002	0.0184	0.0003	0.007	1.909	2.623	2.526
	DEH JAS 012_4	446	342		0.65	0.02	0.0002	5.737E−06	0.0464	0.0007	0.0860	0.0013	0.117	0.396	0.733	0.568

Notes: The He age uncertainties are 1σ propagated from U, Th, and ^{4}He analytical uncertainties and underestimate true He age uncertainties due to alpha-ejection. The U-Th concentrations are approximations calculated from the U-Th masses divided by the Fe-oxide aliquot mass.

[1] The Fe-oxide aliquot mass is an approximation calculated using the measured grain dimensions of each aliquot, assuming an ellipsoid volume and a goethite specific gravity of 4.3 gm/cm^3.

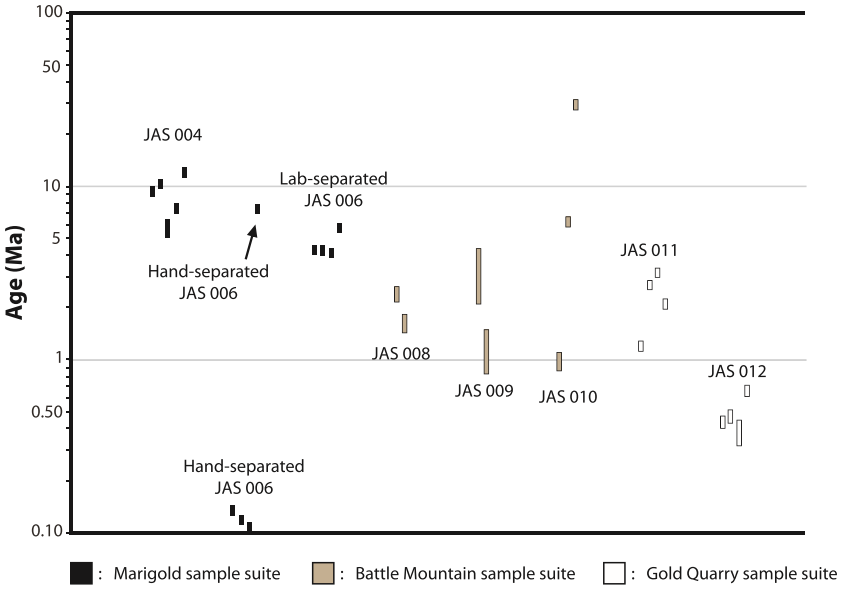

Fig. 11. Fe-oxide (U-Th)/He dates from Marigold, Battle Mountain, and Gold Quarry jasperoid samples.

may be a more efficient discriminator between mineralized and unmineralized jasperoids.

6.2. Fe-oxide (U-Th)/He dates

The (U-Th)/He results reveal a range of dates between 29.4 ± 0.5 Ma and 0.11 ± 0.01 Ma (Table 4; Fig. 11) and display both intra- and intersample He date variation. We quantify the intrasample variation with the relative standard deviation (RSD) of aliquot dates within a single sample. Table 6 compiles the Fe-oxide aliquot data necessary to evaluate the possible causes of date variation. In the subsections below, we focus our discussion on the causes of the observed intrasample date variation, acknowledging that any one of these factors may also contribute to intersample date variation.

6.2.1. He implantation

If interstitial U-Th bearing mineral phases such as clays, apatite, or zircon are present, radioactive decay in these minerals can generate and implant "parentless" He in nearby Fe-oxide aggregates (Evenson et al., 2014), causing date variation. Our preliminary SEM imaging indicated the presence of apatite and zircon grains, so we targeted areas showing only Fe-oxides and silica in the aliquots prepared by microdrilling and hand separation. However, we cannot rule out the presence of U-Th phases below the plane of SEM analysis, or in the aliquots separated by crushing and EPD.

Most of our samples do not show strong negative age-effective uranium (eU) trends (R^2 values range from 0.03 to 0.54; Fig. 12), so we infer that those dates have not been affected by He implantation (Murray et al., 2014). However, our eU concentrations are only approximate values, based on the measured grain dimensions, an assumed ellipsoid volume, and a goethite specific gravity of 4.3 g/cm^3 to calculate the Fe-oxide grain mass necessary to convert U and Th masses to concentrations (Table 4), as opposed to moles relative to Fe (e.g. Reiners et al., 2014). Our eU calculations are most accurate for aliquots with coarse or tightly packed Fe-oxides, but likely underestimate the eU concentrations in aliquots with fine and disseminated Fe-oxides, as the calculations do not account for larger volumes of interstitial phases such as silica. Aliquots with low eU values will be most influenced by He implantation, because an increase in foreign He will dramatically increase the age-eU ratio.

Despite the absence of strong negative age-eU trends within samples, two individual aliquots display older He dates with relatively low eU concentrations, suggesting these aliquots may have been affected by He implantation. In DEH JAS 010, an aliquot with 7.73 ppm eU corresponds to an He date of 29.4 ± 0.5 Ma, the oldest age in our dataset (Table 6; Fig. 12). Similarly, a single aliquot from DEH JAS 006 HS with 2.85 ppm eU corresponds to an He date of 7.36 ± 0.10 Ma. In comparison, the remaining aliquots from DEH JAS 006 HS have eU concentrations which are an order of magnitude larger, yet associated with much younger ages ranging from 0.14 ± 0.01 to 0.11 ± 0.01 Ma (Table 6; Fig. 12).

6.2.2. Parent isotope exchange

Fluid interaction may affect the radionuclide concentrations of the (U-Th)/He isotope system in Fe-oxides (Reiners et al., 2014). If fluids such as groundwater contain dissolved U-Th they could facilitate open-system behavior for parent isotopes by contributing U-Th to the Fe-oxides; conversely, if the fluids are undersaturated with respect to U-Th, they could leach U-Th from the Fe-oxides (Thompson et al., 2003; Borsato et al., 2005; Reiners et al., 2014). Addition of U-Th can generate either a positive or a negative age-eU trend, depending on the initial eU concentration of the Fe-oxide grain and how eU is added to the system. Variable amounts of eU added over time or instantaneously

Table 5
Prospectivity features identified by this study are integrated with those from previous research.

Prospectivity Characteristic		Favorable	Authors
Fe-oxide characteristics		Acicular goethite crystals (<1–4 μm) Chemical zonation Presence of dissolution pits in Fe-oxide crystals, especially where zoned	This study
Jasperoid color		Maroon; light to dark brown Variegated color	Lovering (1972) Theodore and Jones (1991)
Silica	Texture	Phaneritic; vuggy; size range of quartz >10X; reticulated	This study; Lovering (1972)
		Xenomorphic; reticulated; quartz veins display drusy and granular textures, zoned	Hofstra (1994)
	Oxygen isotopes	$\delta^{18}O_{H2O}$: −19 to 10‰; $\delta^{18}O$: 1.1–15.2‰; mixing between highly exchanged and unexchanged meteoric water	Hofstra (1994)
		$\delta^{18}O$: −5‰	Emsbo (1999)
		$\delta^{18}O$: −3.7 to 24.5‰; mixing between highly exchanged and unexchanged meteoric water	Yigit et al. (2006)
	Fluid inclusions	Minimum homogenization temperatures of 120–260 °C; 0–10 wt% NaCl; CO_2-H_2S present	Hofstra (1994)
		Fluid 1: homogenization temperatures of 200–230 °C, 2–6 wt.% NaCl; H_2S present Fluid 2: homogenization temperatures of 175–190 °C; 0–1 wt% NaCl	Emsbo (1999)
	Cathodoluminescence	Mottled and zoned; brick red and blue to gray and black	Hofstra (1994)
		Non-luminescent; very slight dark blue color Late-ore stage quartz: zoned, greenish blue to bluish green; crosscut by bright light green	Emsbo (1999)
Indicator elements		Au, Ag, As, Sb, Pb, W, Tl, U	This study
		Ag, As, Bi, Cu, Fe, Ga, In, Mo, Sn, Zn	Lovering (1972)[1]
		Factor 1: Au-Ag-Sb-SiO_2-As-Pb Factor 2: W-B-V-Zn-Co-Au-CaO-Ni-Mn-Cu	Holland et al. (1988)[2]
		Au, Ag, Sb, Mo, Ba, Ni, P, Mn	Nelson (1990)
		Au, Ag, As, Cu, Pb, Sb, Zn	Theodore and Jones (1991)[3]
		Au, As, Hg, Sb, Tl, Ba	Yigit et al. (2006)
Pre-jasperoid alteration minerals		Calcite, dolomite, apatite, pyrite, carbon, mica, zircon, rutile	Hofstra (1994)
		Pyrite	Lovering (1972)
Syn-jasperoid alteration minerals		Pyrite, stibnite	Emsbo (1999)
		Pyrite, barite, gold	Hofstra (1994)
Post-jasperoid alteration minerals		Goethite, jarosite	Lovering (1972)
		Goethite	This study

[1] Lovering (1972) did not analyze or report Au concentrations, preventing a direct comparison of Au content and the characteristics he identified as favorable for mineralization.
[2] Holland et al. (1988) did not analyze for U.
[3] Theodore and Jones (1991) did not analyze for U and W.

to Fe-oxide grains with a constant initial eU concentration will produce a negative trend (Reiners et al., 2014). By contrast, a constant amount of eU added continuously or instantaneously to Fe-oxides with a range of initial eU concentrations will produce a positive trend (Reiners et al., 2014). Removal of U-Th would appear as lower eU values and artificially older He dates.

We plot the eU concentrations of aliquots against He dates (Fig. 12) and generally observe no trend (R^2 values range from 0.03 to 0.54), suggesting that U-Th addition or removal is not responsible for the observed date variation. The exceptions are three hand-separated aliquots from DEH JAS 006. Compared to the rest of the data from this sample, these aliquots show high eU and extremely young dates (0.14 ± 0.01 Ma to 0.11 ± 0.01 Ma; Fig. 12), which implies late-stage eU addition (Reiners et al., 2014). Late addition of U-Th leads to artificial younging of He dates, and further complicates date calculations as U will be out of secular equilibrium in aliquots whose He dates are younger than 1 Ma (Monteiro et al., 2014).

6.2.3. Closure temperature sensitivity

The Fe-oxides in our jasperoid samples do not generally occur as single, large crystals but rather as polycrystalline aggregates (e.g., Farley and Flowers, 2012). Each individual crystal in the aggregates serves as its own He diffusion domain (Evenson et al., 2014; Farley, 2018; Jensen et al., 2018). Metrics of temperature sensitivity, such as closure temperature and the PRZ, vary as a function of the grain size distribution within the polycrystalline aliquots, increasing with increasing grain size as coarse crystals retain more of their He budget over their lifetime than finer grains

Table 6
Fe-oxide aliquot data required to assess the causes of intrasample Fe-oxide (U-Th)/He He date variation.

	Aliquot mineralogy and morphology Fe-oxide grain size and spacing	Aliquot sample context	Calculated T_c (°C)	(U-Th)/He dates (Ma)	Intrasample dispersion (RSD)	eU-Age trend R^2-value	Intrasample Variation
Marigold							
DEH JAS 004	Goethite; platelet; aggregates ≤125 μm wide; aggregate spacing: 10–30 μm	Clustered aggregates	28–37	5.73 ± 0.42 7.41 ± 0.12 9.33 ± 0.17 10.21 ± 0.18 11.92 ± 0.23	24.2%	No trend $R^2 = 0.15$	**Closure temperature sensitivity**: fractional He loss plot (**Fig. 13**) indicates sample falls within the partial retention zone at near surface conditions and has lost ~10% He.
DEH JAS 006 HS Hand-separated	Goethite; bladed; crystals 500 nm to 20 μm long; aggregates >500 μm long	Fe-oxide coating on silica? Coarse aggregate? Vein fill?	79–121	0.11 ± 0.10 0.12 ± 0.10 0.14 ± 0.10 7.36 ± 0.10	162.4%	Negative trend; artifically high R^2 value due to magnitude difference between single aliquot and remainder of population: causes line of best fit to resemble a two aliquot sample $R^2 = 0.95$	**He implantation**: single aliquot with low eU and high age **(U-Th) addition:** three aliquots with high eU and extremely young age, negative eU-age trend
DEH JAS 006 LS EPD-separated	Goethite; bladed; crystals 500 nm–20 μm long; aggregates > 500 μm long	Vein fill	79–121	4.09 ± 0.07 4.24 ± 0.06 4.25 ± 0.06 5.76 ± 0.08	14.9%	No trend $R^2 = 0.10$	**Aliquot scale variation in He kinetics and thermal history**: minimal He date variation; sample does not appear susceptible to any other causes
Battle Mountain							
DEH JAS 008	Goethite; blocky; aggregates ≤50 μm wide; aggregate spacing: cm-scale	Widely disseminated aggregate	70–99	1.61 ± 0.12 2.37 ± 0.13	19.2%	Two aliquot sample, cannot identify a trend	Insufficient aliquot information
DEH JAS 009	Goethite; blocky; aggregates ≤50 μm wide; aggregate spacing: cm-scale	Widely disseminated aggregate	37–67	1.14 ± 0.28 3.16 ± 0.97	47.0%	Two aliquot sample, cannot identify a trend	Insufficient aliquot information
DEH JAS 010	Goethite; polygonal plates; aggregates ≤800 μm wide; aggregate spacing: 100's μm	Fe-oxide coating on silica? Coarse aggregate?	51–76	0.97 ± 0.07 6.20 ± 0.13 29.4 ± 0.5	101.3%	No trend $R^2 = 0.11$	**He implantation:** low eU, high age
Gold Quarry							
DEH JAS 011	Goethite; mixed botryoidal and acicular; massive Fe-oxide material; individual aliquots ~ 350 μm wide;	Weathering rim	77–110	1.19 ± 0.03 2.07 ± 0.04 2.68 ± 0.03 3.16 ± 0.04	32.4%	No trend $R^2 = 0.03$	**Multiple Fe-oxide morphologies and/or generations:** mixture of acicular and botryoidal morphologies; may indicate multiple Fe-oxide generations; sample does not appear susceptible to any other causes
DEH JAS 012	Goethite; acicular; aggregates ≤200 μm; aggregate spacing: 25–50 μm	Disseminated aggregate	75–98	0.38 ± 0.10 0.43 ± 0.10 0.46 ± 0.10 0.65 ± 0.10	21.5%	No trend $R^2 = 0.54$	**Alpha-ejection:** fine individual Fe-oxide crystal grain size and aggregate spacing near alpha-stopping distance

(Farley and Flowers, 2012; Evenson et al., 2014; McDermott et al., 2017). For example, given a 10 °C/Myr cooling rate and typical Fe-oxide dimensions, the closure temperature for hematite varies between ~25 and 250 °C (Farley and Flowers, 2012; Farley, 2018) and the closure temperature for goethite varies between ~20 and 125 °C (Shuster et al., 2005; Waltenberg, 2013; Reiners et al., 2014; Garcia et al., 2017). Therefore, the range of temperatures sensitivities for a bulk aliquot with multiple crystals and/or aggregates can be fairly restrictive or broad depending on the intrasample grain size variability (Evenson et al., 2014; Ault et al., 2015; McDermott et al., 2017). In order to assess the range of temperatures over which our samples progressed from fully open to closed for He diffusion, we used the grain half-widths and He kinetics of Table 3 to calculate the 0.9 and 0.1 fractional loss contours for each of the jasperoid Fe-oxide morphologies that we observed in thin section (Fig. 13). Importantly, for nearly all jasperoid Fe-oxide morphologies, less than 10% He loss would occur at near-surface conditions (temperatures of 20 °C; Fig. 13), which suggests that, if our samples were formed by redox meteoric fluids in a near-surface environment, then they were nearly fully closed to diffusive He loss after formation. Goethite platelets in aliquots from DEH JAS 004 are the sole exceptions. Fig. 13B reveals an aliquot from DEH JAS 004 is likely to lose 10% of its He budget if held at 20 °C for 1 Ma and up to 80% of its He if held at this temperature for 10 Ma. The calculated closure temperatures for aliquots from DEH JAS 004 range from 28-37 °C, which are some of the lowest calculated closure temperatures from our dataset (Table 3). The He dates from DEH JAS 004 display a broad range from 10.21 ± 0.18 to 5.73 ± 0.42 Ma, suggesting that diffusive He loss has occurred. For this sample, we interpret that variable grain size and corresponding temperature sensitivity is the dominant cause of the observed intrasample date variation.

6.2.4. Alpha-ejection

Alpha-ejection can cause artificial younging of He dates. Total He loss will occur if the Fe-oxide crystals are smaller than the alpha-stopping distance and spaced too far apart for He implantation to balance the He loss. The stopping distance of the He atom ranges between 13 and 18 μm for the ^{238}U and ^{232}Th series in hematite and goethite; however, even Fe-oxide crystals and aggregates up to 40 μm in diameter will require a ~60% age correction (Ketcham et al., 2011). In fine-grained Fe-oxides, the stopping distance commonly exceeds the dimensions of any individual oxide crystal (Evenson et al., 2014; Farley, 2018; Jensen et al., 2018). Jasperoids are especially susceptible to He loss through alpha-ejection because the interstitial mineralogy between Fe-oxide crystals or aggregates is predominantly silica. Helium diffusion from quartz occurs rapidly and He can escape the system entirely in 10^3–10^4 years at surface temperatures (Shuster and Farley, 2005; Tremblay et al., 2014).

We suggest that alpha-ejection may be a major control on date variation in jasperoids that contain fine-grained, disseminated Fe-oxide crystals. In DEH JAS 012, rounded aggregates up to 25 μm in diameter are composed of submicron acicular crystals, and the aggregates themselves are spaced 5–15 μm apart (Fig. 10C). All aliquot He dates from this sample are younger than 1 Ma (0.65 ± 0.02 Ma to 0.38 ± 0.04 Ma). As mentioned in Section 6.2.2, He dates younger than 1 Ma imply that U has yet to reach secular equilibrium (Monteiro et al., 2014). However, we suspect the aliquots from DEH JAS 012 have lost significant amounts of He through alpha-ejection and that therefore the He dates are artificially young. The fractional loss contours for acicular morphologies (Fig. 13C) such as the Fe-oxides in DEH JAS 012, provide further evidence that alpha-ejection is the dominant cause of He date variation in this sample. At 20 °C, the system is already below the 0.1 He loss contour, indicating the system is essentially closed to He diffusion. We conclude that alpha-ejection is therefore most likely responsible for the He date variation of this sample, as alpha-ejection is decoupled from diffusivity. We anticipate that nearly all our samples have lost some amount of He through alpha-ejection and require at least partial correction. Disaggregated aliquots from DEH JAS 006 may be an exception, as the EPD mineral separate lacks interstitial mineral phases and is nearly pure Fe-oxide material, which enabled us to select grains whose dimensions greatly exceeded the alpha-stopping distance. These aliquots also display the least intrasample variability within our dataset (intrasample RSD 14.9%; Table 6).

Researchers have attempted to correct for He loss from Fe-oxides to surrounding phases (Evenson et al., 2014; Reiners et al., 2014). However, these methods rely on average or bulk values for the size, shape, and spacing of Fe-oxide crystallites, preventing the development of a standardized correction factor. We report uncorrected dates, following the approach of previous studies on aliquots containing varying amounts of Fe-oxide and silica material (Farley and Flowers, 2012; Reiners et al., 2014; Ault et al., 2015; Garcia et al., 2017; McDermott et al., 2017; Moser et al., 2017; Calzolari et al., 2018; Jensen et al., 2018). Using X-ray computed microtomography (micro-CT) and a granular Fe-oxide aggregate from DEH JAS 008, Huber et al. (2019) developed a new method to calculate an alpha-ejection loss correction factor for complex Fe-oxide aggregate morphologies. The aggregate in Huber et al. (2019) was selected because it represented a disseminated Fe-oxide sample that did not lend itself to simple assumptions for alpha-ejection correction. That is, the aggregate consisted of a continuous mass of Fe-oxide crystallites with a collective diameter of approximately 100 μm, but with a complex morphology that created a high irregular spacing between individual crystallites. In this sense, the aggregate was an extreme example of grains susceptible to He loss through alpha-ejection, and a correction factor of approximately 0.25 was necessary to correct for the effects of alpha-ejection in their aliquot. We take this correction factor as a conservative estimate for our own dataset.

6.2.5. Fe-oxide mineralogy, morphology, and generations

Next we consider causes of He date variation specific to the Fe-oxide aliquots themselves. First we consider whether Fe-oxide mineralogy may contribute to the observed date variation. Protolith mineralogy, geochemistry, and composition of the causative alteration fluid can produce a variety

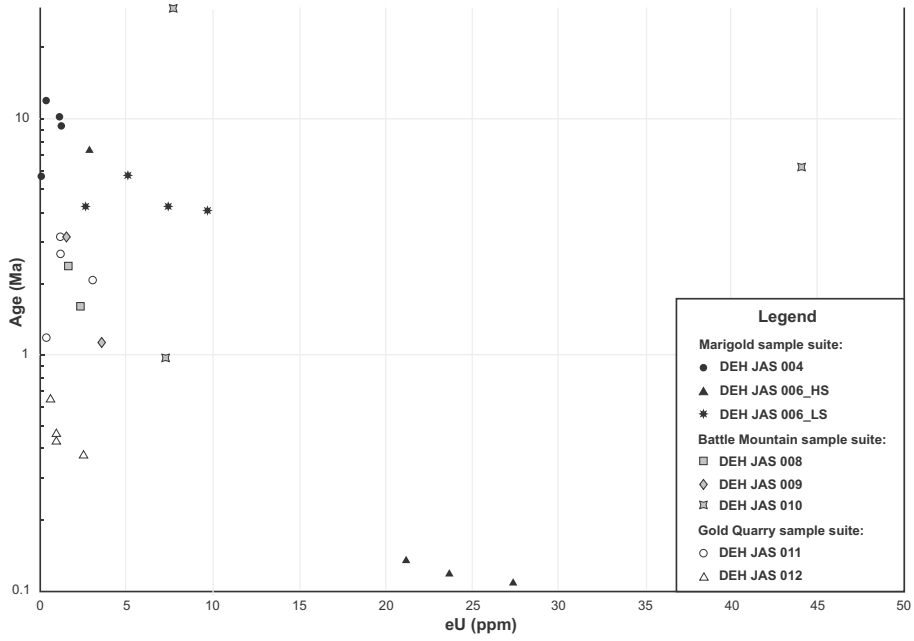

Fig. 12. Fe-oxide (U-Th)/He ages as a function of eU (U + 0.235Th) concentration (ppm). To calculate eU concentrations, we converted the U-Th masses to concentrations using the measured aliquot grain dimensions, an assumed ellipsoid volume, and a goethite specific gravity of 4.3 g/cm^3 to calculate a Fe-oxide grain mass. Black symbols represent the Marigold sample suite, grey symbols represent the Battle Mountain sample suite, and white symbols represent the Gold Quarry sample suite. These samples show generally no eU-age correlation, suggesting little to no U-Th was added or removed from the system.

of Fe-oxide minerals in jasperoids. Each Fe-oxide mineral species has its own He diffusion kinetics, which creates the possibility of both intersample and intrasample He date variation. To avoid introducing this possible source of date dispersion, we dated solely aliquots which appeared to contain only goethite when imaged with SEM. Therefore we infer that the influence of this factor is relatively minor.

Second, we consider the natural heterogeneity of Fe-oxide crystal morphologies. A single Fe-oxide mineral species can develop various crystal morphologies due to a variety of factors: saturation of the system with respect to Fe, anisotropic growth of different crystal faces, and lattice strain due to differing radii, electric charges, and electronegativities during ion substitution (Cornell and Schwertmann, 1996; Qiu et al., 2016). We do not think Fe-oxide crystal morphology contributes to intrasample He date variation for most samples in our dataset, as we imaged mineral separates with SEM to ensure all aliquots from a single sample contained Fe-oxides of the same morphology. The exception is sample DEH JAS 011, whose aliquots contain a mixture of acicular and botryoidal Fe-oxide morphologies from the interior of a weathering rind (Table 6; Fig. 9A, B); this mixture may contribute to the intrasample He date variation (RSD = 32.4%). Fe-oxide morphology may also contribute to intersample date dispersion in our dataset. There was relatively little overlap in morphologies among the samples that we dated (Table 6), so the influence of this factor is difficult to assess. However, we note that there is an order of magnitude difference between the dates from the two samples with bladed goethite aliquots (DEH JAS 006 HS and DEH JAS 006 LS), suggesting that morphology alone does not provide the dominant control on He date variation (Table 6).

Third, we consider the possibility of multiple Fe-oxide generations in our samples. Each He date may represent a unique Fe-oxide population. The distinct acicular and botryoidal morphologies in aliquots from DEH JAS 011 may represent different Fe-oxide generations and, based on distinct brightnesses observed in BSE, the botryoidal morphology itself may have two generations (Fig. 9A). This mixture may further contribute to the intrasample He date variation of this sample (RSD = 32.4%), thus we include sampling of different Fe-oxide generations as a potential cause of date variation in our dataset.

7. CONCLUSIONS

This study comprises the first detailed characterization of Fe-oxides in jasperoids. Previous work focused on the silicification associated with jasperoid alteration but neglected to consider the Fe-oxides, which are ubiquitous in jasperoids. Our work shows that limited quantities of finely disseminated Fe-oxides are able to cause strong dark red to brown coloration in jasperoids. The Fe-oxides occur in a variety of styles, from extremely fine-grained disseminated crystals to coarser aggregates and vein fill material. Scanning electron microscopy is mandatory to characterize the Fe-oxides, as many of the features and textures are visible only at the micron scale. In our limited sample set, the Fe-oxide characteristics associated with increased Au prospectivity include extremely fine grain size (<100 nm), feathery to acicular crystal morphology, concentric zona-

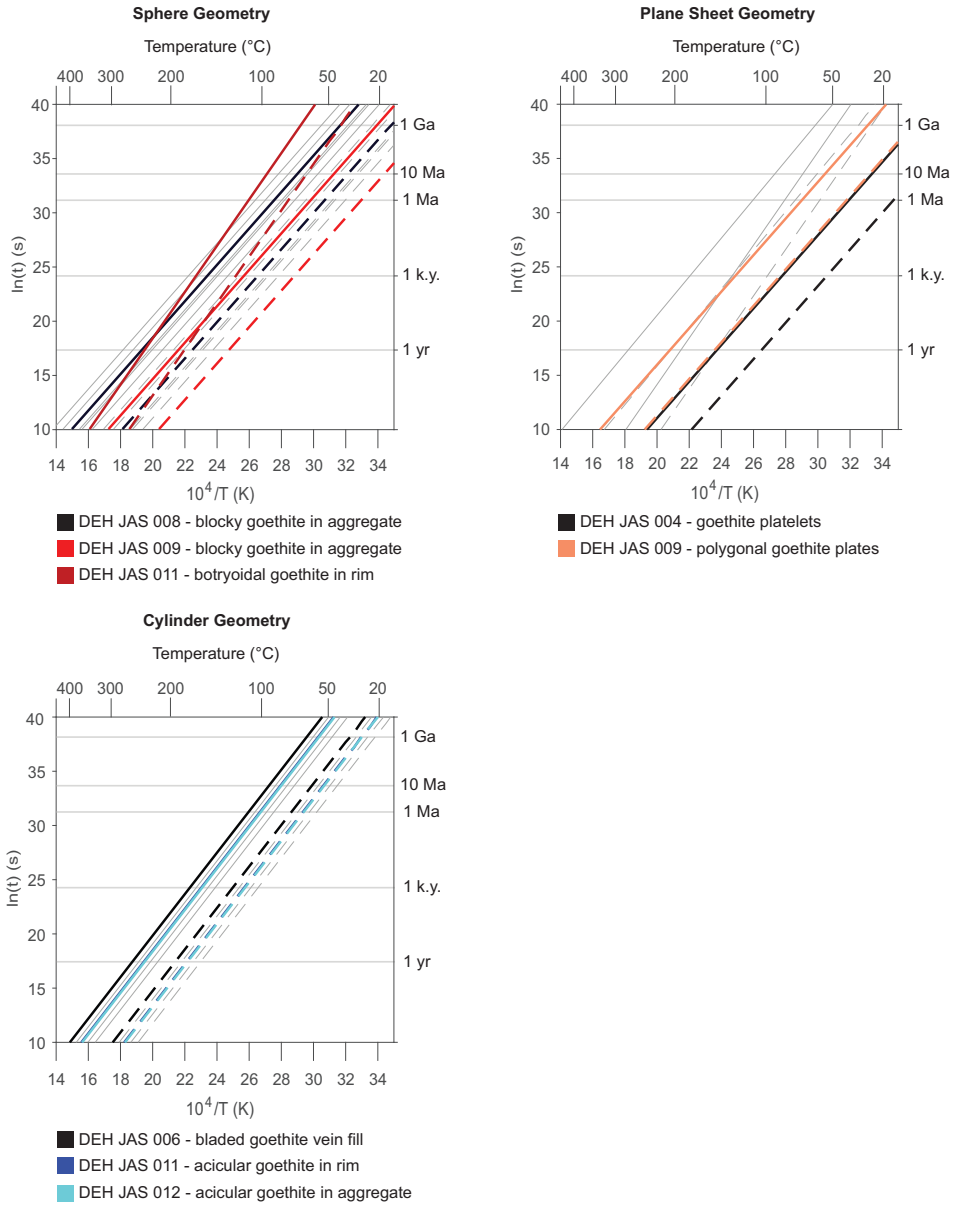

Fig. 13. Goethite 0.9 and 0.1 fractional loss contours as a function of time (t) and the inverse of temperature (T) calculated from a square-pulse heating event. For each Fe-oxide morphology plotted, calculations use the same activation energies (E_a) and diffusion domain length scales (a) as the calculations in Table 3. Dated morphologies are plotted in bold. Undated morphologies are plotted in grey to portray the range of possible He retention behaviors and to allow for comparison with the behavior of dated samples.

tion from hematite to goethite, and botryoidal textures. In our jasperoid samples, Au concentration is positively correlated with Ag, As, Pb, Sb, Tl, W, and U at the hand sample scale.

Application of the (U-Th)/He method to jasperoid Fe-oxides is complicated due to the natural variability of jasperoids themselves. Jasperoids display varied textures, mineralogies, and oxide generations within a single outcrop or hand sample, which hinders reproducibility. Individual jasperoid Fe-oxide crystals are generally fine-grained (<10 μm) and disseminated, which makes them susceptible to alpha-ejection He loss and precludes the use of hand separation methods. If coarse Fe-oxide crystals or aggregates exist within a sample, we recommend using EPD separation followed by Frantz separation, in order to isolate a pure Fe-oxide separate. This facilitates selection of Fe-oxide aliquots whose dimensions exceed the alpha-stopping distance, mitigating the need for an alpha-ejection correction factor. Especially in samples separated by EPD where the spatial context of the Fe-oxide aliquots within the sample is lost, it is necessary to identify U-Th bearing mineral phases such as apatite, zircon, or clays in order to assess whether the dates may have been affected by He implantation. Imaging of the sample with SEM prior to and post-aliquot separation can be used to identify these minerals. However, SEM only captures information in two

dimensions, and three-dimensional methods such as micro-CT reveal the internal structure of an aliquot according to attenuation contrast rather than mineral species (e.g., Huber et al., 2019). In order to minimize sources of date dispersion, jasperoid samples should contain no more than one Fe-oxide generation, but the natural heterogeneity of Fe-oxide mineral species makes this a difficult goal to achieve. Although groundwater interaction may alter the eU concentrations of jasperoid Fe-oxides, the magnitude of this effect on the He dates cannot be determined empirically prior to (U-Th)/He analysis. In order to ensure that diffusive He loss has not occurred at near surface conditions or the conditions at which supergene jasperoid alteration is anticipated to have occurred, we recommend calculating the closure temperatures of the aliquot-specific Fe-oxide morphologies following aliquot separation. Depending on the Fe-oxide morphologies available in a jasperoid sample, it may not be possible to avoid open system behavior.

Given the above challenges, multiple factors likely led to intrasample date variation in our samples, including: He implantation, parent isotope exchange, susceptibility to near surface He loss, alpha-ejection, Fe-oxide mineralogy, and multiple Fe-oxide generations. Multiple factors may cause the observed He date variation within a single sample, and it is difficult to quantify their relative contributions. The submicron and acicular Fe-oxide morphologies specific to our Au-bearing samples contributed to our inability to evaluate the potential relationship between Fe-oxide He date and Au concentration. Although the Fe-oxide He dates from our Au-bearing jasperoid samples did not provide any information on processes related to mineralization, we suggest that the Fe-oxide (U-Th)/He method could serve as a useful tool during exploration for ore deposits containing hypogene Fe-oxides.

Declaration of Competing Interest

The authors declare that they have no known competing financial interests or personal relationships that could have appeared to influence the work reported in this paper.

ACKNOWLEDGMENTS

We thank P. Reiners, U. Chowdhury, and E. Able (University of Arizona) for assistance with (U-Th)/He analyses and V. Valencia at Zirchron LLC for sample separation. Comments from A. Ault and two anonymous reviewers greatly improved the manuscript. NSF EAGER awards to EH (1641142) and WRG (1641138) and a NSF CAREER award to EH (1752756) supported this research. We gratefully acknowledge Newmont Goldcorp Corporation and SSR Mining Inc. for access to sampling sites and logistical support.

APPENDIX A

Scanning electron microscopy

The SEM analyses were conducted at the Department of Geology and Geological Engineering at the Colorado School of Mines using a TESCAN MIRA3 LMH Schottky field emission scanning electron microscope (FE-SEM) equipped with a Bruker XFlash® 6/30 silicon drift detector for energy-dispersive X-ray spectrometry (EDX) and a single-crystal YAG backscatter electron detector. Backscattered electron (BSE) images were collected under an accelerating voltage of 8 or 15 kV, BI of 11, with a working distance of 10 mm.

Geochemistry

Whole rock geochemistry samples were crushed in two stages: first, to reduce 90% of material to less than 2 mm to pass through a 10 mesh sieve, then 250 g of that material was riffle split and pulverized using mild steel until 95% of the material would pass through a 105 μm cleaner sand.

The pulverized samples were then mixed with lithium metaborate and lithium tetraborate and fused in an induction furnace to a molten bead. The molten melt was mixed in a 5% nitric acid solution until completely dissolved; the preliminary fusion step was necessary to ensure complete dissolution in the nitric acid. The resulting solution was analyzed for Al_2O_3, CaO, Fe_2O_3, K_2O, MgO, MnO, Na_2O, P_2O_5, SiO_2, TiO_2, Ba, Be, Co, Cr, Sc, Sr, V, Y, and Zr using Fusion Inductively Coupled Plasma-Mass Spectrometry (ICP-MS). Fused samples were analyzed on a combination simultaneous/sequential Thermo Jarrell-Ash ENVIRO II ICP or a Varian Vista 735 ICP. To measure the remaining trace elements (As, Bi, Cs, Ga, Ge, Hf, In, Mo, Nb, Rb, Sb, Sn, Ta, Th, Tl, W, U, and the rare earth elements), fused samples were diluted and analyzed by Perkin Elmer Sciex ELAN 6000 ICP/MS.

Instrumental Neuron Activation Analysis (INAA) was used to analyze for Au, As, Br, Cr, Ir, Sb, Sc, and Se. During INAA, a 30 g aliquot was encapsulated in a polyethylene vial and irradiated with flux wires and an internal standard at a thermal neutron flux of $7 \times 1012n\ cm^{-2}\ s^{-1}$. After a 7-day period to allow Na-24 to decay, the samples were counted on a high purity Ge detector.

Total Digestion ICP-MS was used to analyze for Ag, Cd, Cu, Ni, Pb, S, and Zn to ensure accurate levels of base metals. During TD-ICP-MS, a 0.25 g sample was digested with four acids beginning with hydrofluoric acid, followed by a mixture of nitric and perchloric acids, heated using precise programmer controlled heating in several ramping and holding cycles which dried the samples. After dryness was attained, samples were brought back into solution using hydrochloric acid. Samples were then analyzed using a Varian Vista 735 ICP.

The Hg Cold Vapor Field Ionization Mass Spectrometry (FIMS) method was used to accurately measure Hg concentrations. During Hg Cold Vapor FIMS, approximately 0.5 g of each sample was digested with aqua regia to leach out soluble compounds. The Hg in the resulting solution was oxidized to the stable divalent form, and an aliquot of the digestion solution was mixed with a potassium permanganate solution. Using the flow injection cold vapor mercury technique, Hg (II) was reduced to mercury vapor using stannous chloride. Argon was bubbled through the mixture of sample, carrier, and reductant solutions in a closed reaction system to liberate and transport the Hg atoms into an absorption cell. Hg was determined via the

absorption of light at 253.7 nm. The maximum amount absorbed, or peak height, is directly proportional to the concentration of mercury atoms in the light path. A Perkins Elmer FIMS 100 was used for the analysis.

Bright phase search

Samples were loaded into the TESCAN-VEGA-3 Model LMU VP-SEM platform and the analyses were initiated using the control program TIMA3. Four EDX spectrometers acquired spectra from each point or particle with a 1 μm beam stepping interval (i.e., spacing between acquisition points), an acceleration voltage of 25 keV, and a beam intensity of 14. The EDX spectra were compared with spectra held in a look-up table, allowing a mineral or phase to be assigned at each acquisition point. The assignment made no distinction between mineral species and amorphous grains of similar composition. Results were output by the TIMA software as a spreadsheet giving the area percent of each composition in the look-up table. The Bright Phase Search constituted point analyses of points with a brightness of at least 60%, a cutoff which restricts the analyses to elements with a higher atomic Z-number, including Au. This procedure generated a BSE map of all the acquisition points identified as gold.

Fe-oxide separation

Several methods were used to separate Fe-oxides from the jasperoid whole rock samples for (U-Th)/He analysis:

(1) A single jasperoid hand sample was reduced to an appropriate size fraction with a sledge hammer and then crushed with a hand held rock crusher. Individual jasperoid grains less than 1 mm were handpicked, cleaned in 10% ethanol alcohol, and set aside to dry.
(2) Three jasperoid hand samples were mechanically crushed to separate Fe-oxides. Crushed grains were sieved into bins of >250 μm, 150–250 μm, 90–150 μm, and <90 μm. Grains from each bin size were processed separately through the Frantz Isodynamic Magnetic Separator with the following settings: 20° longitudinal tilt, 3-6° transverse tilt at an amperage of 0.7–0.8 amps. The waste product was reprocessed two to three times with the Frantz Isodynamic Magnetic Separator to capture any additional Fe-oxide material that was missed in the first round. Separated grains were then re-run to high-grade desired material. Transverse tilt and amperage were adjusted based on grain size and the relative proportion of magnetic particles.
(3) Three jasperoid hand samples were sliced into 2 mm-thick slabs using a rock saw. One hand sample was halved and also separated using the fourth method. Material from Fe-oxide veinlets was isolated using a microdrill, a dental pick, and tweezers. Fe-oxide material was crushed until the grains would fit within a Nb tube.
(4) One duplicate jasperoid hand sample was separated for Fe-oxides by Zirchron LLC, in Tucson AZ. The sample was unpacked and pressure washed with water to remove any debris or foreign material. Sample rock fragments were placed in the sample chamber of an Electro Pulse Disaggregator (EPD, Marx generator) modified from a CNT SPARK-3. Water was added and electrical pulses were applied at 1 Hz repetition and discharges of 230 kV for 10–15 minutes. Sample materials finer than the 500 μm stainless steel mesh sieve were collected in a disposable plastic bag. The coarser material remaining in the crush chamber was collected and dried for further size reduction by traditional methods (rock crusher and pulverizer), if necessary. The collected material (<500 μm) was sieved twice more through 350 μm and 20 μm nylon disposable mesh sieves. The size fraction >350 μm was added to the <500 μm material and the size fraction finer than 20 μm was discarded. Individual Fe-oxide grains were extracted using one step heavy liquids, followed by Frantz paramagnetic separation at 1 amp.

Fe-oxide (U-Th)/He analysis

Analytical methods followed those described in Reiners et al. (2014) and consisted of diode, Nd:YAG, or CO_2 laser heating, cryogenic purification, and quadrupole mass-spectrometry for ^{4}He analysis; and isotope-dilution high-resolution-inductively coupled plasma-mass spectrometry (HR-ICP-MS) for U and Th analysis. Nb-enveloped Fe-oxide aliquots were dissolved in pressure digestion vessels (Parr bombs), and U-Th was measured on an Element2 high-resolution ICP-MS, following the same methods used for zircon (U-Th)/He dating (Reiners, 2005).

Closure temperature calculations

To gain a sense of the temperature sensitivity of individual jasperoid Fe-oxide samples, we iterated the closure temperature calculation of Dodson (1973):

$$T_c = \frac{E_a}{R \ln\left[\frac{ART_c^2 D_0}{a^2 E_a \left(\frac{dT}{dt}\right)}\right]}$$

where

T_c = closure temperature (K)
E_a = activation energy, dependent on Fe-oxide mineralogy and crystal morphology
For goethite: 178.4 kJ/mol (Shuster et al., 2005); 140 kJ/mol (Reiners et al., 2014); 159 kJ/mol (Garcia et al., 2017)
For hematite: 157 kJ/mol (Farley and Flowers, 2012)
R = gas constant; 0.008314 kJ/K•mol
A = unitless geometry dependent term: 8.65 (plate sheet), 27 (cylinder); 55 (sphere)
D_0 = frequency factory, dependent on Fe-oxide mineralogy and crystal morphology
For goethite: $e^{8.5}$ cm^2/s (Shuster et al., 2005); $e^{-2.3}$ cm^2/s (Reiners et al., 2014); $e^{-4.8}$ cm^2/s (Garcia et al., 2017)

For hematite: 2.2×10^{-4} cm^2/s (Evenson et al., 2014)
a = measured grain dimension (cm); plate half-widths were measured for platelet, bladed, and acicular morphologies; crystal radii were measured for granular, spherical, anhedral, and aggregate morphologies
dT/dt = cooling rate; 3.16881E−13 (K/s)

The closure temperature equation was applied iteratively to each individual grain measurement per sample. The minimum, maximum, and mean grain half-widths and corresponding closure temperatures are reported in Table 2 for each Fe-oxide crystal morphology recognized per jasperoid sample.

APPENDIX B. SUPPLEMENTARY MATERIAL

Supplementary data to this article can be found online at https://doi.org/10.1016/j.gca.2020.07.014.

REFERENCES

Ault A. K., Frenzel M., Reiners P. W., Woodcock N. H. and Thomson S. N. (2016) Record of paleofluid circulation in faults revealed by hematite (U-Th)/He and apatite fission-track dating: An example from Gower Peninsula fault fissures, Wales. *Lithosphere* **8**, 379–385.

Ault A. K., Reiners P. W., Evans J. P. and Thomson S. N. (2015) Linking hematite (U-Th)/He dating with the microtextural record of seismicity in the Wasatch fault damage zone, Utah, USA. *Geology* **43**, 771–774.

Bakken B. M. and Einaudi M. T. (1986) Spatial and temporal relations between wall rock alteration and gold mineralization: main pit, Carlin gold mine, Nevada, USA. In *Gold '86 Symposium. Toronto* (ed. A. J. Macdonald), pp. 388–403.

Borsato A., Quinif Y., Bini A. and Dublyansky Y. (2005) Open-system alpine speleothems: implications for U-series dating and paleoclimate. *Stud. Trent. Sci. Nat. Acta Geol.* **80**, 71–83.

Braun J., van der Beek P. and Batt G. (2006) *Quantitative Thermochronology: Numerical Methods for the Interpretation of Thermochronological Data*. Cambridge University Press, Cambridge.

Cail T. L. and Cline J. S. (2001) Alteration associated with gold deposition at the Getchell Carlin-type gold deposit, north-central Nevada. *Econ. Geol.* **96**, 1343–1359.

Calzolari G., Rossetti F., Ault A. K., Lucci F. and Olivetti V. (2018) Tectonophysics hematite (U-Th)/He thermochronometry constrains intraplate strike-slip faulting on the Kuh-e-Faghan Fault, central Iran. *Tectonophysics* **728–729**, 41–54.

Chakurian A. M., Arehart G. B., Donelick R. A., Zhang X. and Reiners P. W. (2003) Timing constraints of gold mineralization along the Carlin trend utilizing apatite fission-track, 40Ar/39Ar, and apatite (U-Th)/He methods. *Econ. Geol.* **98**, 1159–1171.

Cline J. S. and Hofstra A. (2000) Ore-fluid evolution at the Getchell Carlin-type gold deposit, Nevada, USA. *Eur. J. Mineral.* **12**, 195–212.

Cline J. S., Hofstra A. H., Muntean J. L., Tosdal R. M. and Hickey K. A. (2005) Carlin-type gold deposits in Nevada: Critical geologic characteristics and viable models. *Econ. Geol.* **100th Anni**, 451–484.

Cornell R. M. and Schwertmann U. (1996) *The Iron Oxides: Structure, Properties, Reactions, Occurrences and Uses*. VCH Publishers, Weinheim; New York; Basel; Cambridge; Tokyo.

Danišík M., Evans N. J., Ramanaidou E. R., McDonald B. J., Mayers C. and McInnes B. I. A. (2013) (U-Th)/He chronology of the Robe River channel iron deposits, Hamersley Province, Western Australia. *Chem. Geol.* **354**, 150–162.

Dodson M. H. (1973) Closure temperature in cooling geochronological and petrological systems. *Contrib. Mineral. Petrol.* **40**, 259–274.

Dominy S. C., Platten I. M. and Raine M. D. (2003) Grade and geological continuity in high-nugget effect gold–quartz reefs: implications for resource estimation and reporting. *Appl. Earth Sci.* **112**, 239–259.

Emsbo P. (1999) *Origin of the Meikle High-grade Gold Deposit from the Superposition of Late Devonian Sedex and mid-Tertiary Carlin-type Gold Mineralization*. Colorado School of Mines.

Emsbo P., Hofstra A. H., Lauha E. A., Griffin G. L. and Hutchinson R. W. (2003) Origin of high-grade gold ore, source of ore fluid components, and genesis of the Meikle and Neighboring Carlin-Type Deposits, Northern Carlin Trend, Nevada. *Econ. Geol.* **98**, 1069–1105.

Evenson N. S., Reiners P. W., Spencer J. E. and Shuster D. L. (2014) Hematite and Mn oxide (U-Th)/He dates from the buckskin-Rawhide detachment system, Western Arizona: Gaining insights into hematite (U-Th)/He systematics. *Am. J. Sci.* **314**, 1373–1435.

Farley K. A. (2018) Helium diffusion parameters of hematite from a single-diffusion-domain crystal. *Geochim. Cosmochim. Acta* **231**, 117–129.

Farley K. A. and Flowers R. M. (2012) (U-Th)/Ne and multidomain (U-Th)/He systematics of a hydrothermal hematite from eastern Grand Canyon. *Earth Planet. Sci. Lett.* **359–360**, 131–140.

Farley K. A. and McKeon R. (2015) Radiometric dating and temperature history of banded iron formation–associated hematite, Gogebic iron range, Michigan, USA. *Geology* **43**, 1083–1086.

Farley K. A., Wolf R. A. and Silver L. T. (1996) The effects of long alpha-stopping distances on (U-Th)/He ages. *Geochim. Cosmochim. Acta* **60**, 4223–4229.

Fithian M. T., Holley E. A. and Kelly N. M. (2018) Geology of gold deposits at the marigold mine, Battle Mountain District, Nevada. In *Divers. Carlin-Style Gold Depos*, 20 (ed. J. L. Muntean).

Fournier R. O. (1985) Silica minerals as indicators of conditions during gold. In *U.S Geological Survey Bulletin 1646*, pp. 15–26.

Garcia V. H., Reiners P. W., Shuster D. L., Idleman B. and Zeitler P. K. (2017) Thermochronology of sandstone-hosted secondary Fe- and Mn-oxides near Moab, Utah: Record of paleo–fluid flow along a fault. *GSA Bull.* **130**, 93–113.

Goldfarb R. J., Hofstra A. H. and Simmons S. F. (2016) Critical elements in Carlin, epithermal, and orogenic gold deposits. In *Rare Earth and Critical Elements in Ore Deposits Society of Economic Geologists*. Littleton, CO, pp. 217–244.

Heim J. A., Vasconcelos P. M., Shuster D. L., Farley K. A. and Broadbent G. (2006) Dating paleochannel iron ore by (U-Th)/He analysis of supergene goethite, Hamersley province, Australia. *Geology* **34**, 173–176.

Hickey K. A., Barker S. L. L., Dipple G. M., Arehart G. B. and Donelick R. A. (2014) The brevity of hydrothermal fluid flow revealed by thermal halos around giant gold deposits: implications for Carlin-Type Gold Systems. *Econ. Geol.* **109**, 1461–1487.

Hofstra A. H. (1994) *Geology and Genesis of the Carlin-type Gold Deposits in the Jeritt Canyon District*. University of Colorado, Nevada.

Hofstra A. H. and Cline J. S. (2000) Characteristics and models for Carlin-type gold deposits. *Rev. Econ. Geol.* **13**, 163–220.

Hofstra A. H., John D. A. and Theodore T. G. (2003) A special issue devoted to gold deposits in Northern Nevada: Part 2. Carlin-type deposits preface. *Econ. Geol.* **98**, 1063–1067.

Holland P. T., Beaty D. W. and Snow G. G. (1988) Comparative elemental and oxygen isotope geochemistry of Jasperoid, in hydrothermal systems. *Econ. Geol.* **83**, 1401–1423.

Huber C., Guenthner W. and Karani H. (2019) A new correction for He loss applied to (U-Th)/He dating of grains with complex shapes and polymineralic aggregates. *Geochem. Geophys. Geosyst.* **20**, 5744–5764.

Huff D. E., Holley E. A. and Guenthner W. R. (2019) Hunting elephants with microanalyses – LA-ICP-MS geo- and thermochronology applied to Carlin exploration. In *Smart Mining: Resources for a Connected World*. Society of Mining, Metallurgy and Mineral Exploration, Denver, p. 365.

Huff D. E., Holley E. A., Lowe J. A., Fithian M. T., Guenthner W. R. and Kaempfer J. (2018) "Distal-Disseminated" deposits in the battle mountain mining district: Possible expressions of a porphyry-Carlin continuum? In *Metals, Minerals, and Society*. Society of Economic Geologists, Keystone, p. 177.

Jensen J. L., Siddoway C. S., Reiners P. W., Ault A. K., Thomson S. N. and Steele-MacInnis M. (2018) Single-crystal hematite (U–Th)/He dates and fluid inclusions document widespread Cryogenian sand injection in crystalline basement. *Earth Planet. Sci. Lett.* **500**, 145–155.

Johnston M. K., Thompson T. B., Emmons D. L. and Jones K. (2008) Geology of the cove mine, Lander County, Nevada, and a genetic model for the McCoy-Cove hydrothermal system. *Econ. Geol.* **103**, 759–782.

Ketcham R. A., Gautheron C. and Tassan-Got L. (2011) Accounting for long alpha-particle stopping distances in (U–Th–Sm)/He geochronology: Refinement of the baseline case. *Geochim. Cosmochim. Acta* **75**, 7779–7791.

Kuehn C. A. and Rose A. W. (1992) Geology and geochemistry of wall-rock alteration at the Carlin gold deposit, Nevada. *Econ. Geol.* **87**, 1697–1721.

Lippolt H. J., Wernicke R. S. and Bahr R. (1995) Paragenetic specularite and adularia (Elba, Italy): Concordant (U + Th)-He and K-Ar ages. *Earth Planet. Sci. Lett.* **132**, 43–51.

Lovering, T.G., 1972. Jasperoid in the United States – Its Characteristics, Origin, and Economic Significance, Washington.

McDermott R. G., Ault A. K., Evans J. P. and Reiners P. W. (2017) Thermochronometric and textural evidence for seismicity via asperity flash heating on exhumed hematite fault mirrors, Wasatch fault zone, UT, USA. *Earth Planet. Sci. Lett.* **471**, 85–93.

Meesters A. G. C. and Dunai T. (2002) Solving the production–diffusion equation for finite diffusion domains of various shapes: Part I. Implications for low-temperature (U–Th)/He thermochronology. *Chem. Geol.* **186**, 333–344.

Monteiro H. S., Vasconcelos P. M., Farley K. A., Spier C. A. and Mello C. L. (2014) (U–Th)/He geochronology of goethite and the origin and evolution of cangas. *Geochim. Cosmochim. Acta* **131**, 267–289.

Moser A. C., Evans J. P., Ault A. K., Janecke S. U. and Bradbury K. K. (2017) (U–Th)/He thermochronometry reveals Pleistocene punctuated deformation and synkinematic hematite mineralization in the Mecca Hills, southernmost San Andreas Fault zone. *Earth Planet. Sci. Lett.* **476**, 87–99.

Muntean, J.L., Davis, D.A., Ayling, B., 2018. The Nevada Mineral Industry 2017.

Murray K. E., Orme D. A. and Reiners P. W. (2014) Effects of U-Th-rich grain boundary phases on apatite helium ages. *Chem. Geol.* **390**, 135–151.

Nelson C. E. (1990) Comparative geochemistry of jasperoids from Carlin-type gold deposits of the western United States. *J. Geochem. Explor.* **36**, 171–195.

Qiu G., Feng X., An P., Liang X., Li W., Tan W., Liu F. and Yin H. (2016) Mechanisms on the morphology variation of hematite crystals by Al substitution: The modification of Fe and O reticular densities. *Sci. Rep.* **6**, 1–10.

Reiners P. W. (2005) Zircon (U-Th)/He thermochronometry. *Rev. Mineral. Geochem.* **58**, 151–179.

Reiners P. W., Chan M. A. and Evenson N. S. (2014) (U-Th)/He geochronology and chemical compositions of diagenetic cement, concretions, and fracture-filling oxide minerals in mesozoic sandstones of the Colorado Plateau. *Bull. Geol. Soc. Am.* **126**, 1363–1383.

Reiners P. W. and Farley K. A. (2001) Influence of crystal size on apatite (U–Th)/He thermochronology: an example from the Bighorn Mountains, Wyoming. *Earth Planet. Sci. Lett.* **188**, 413–420.

Ressel M. W. and Henry C. D. (2006) Igneous geology of the Carlin trend, Nevada: Development of the Eocene plutonic complex and significance for Carlin-type gold deposits. *Econ. Geol.* **101**, 347–383.

Rota J. C. and Hausen D. M. (1991) Geology of the Gold Quarry mine. *Ore Geol. Rev.* **6**, 83–105.

Saunders J. A. (1994) Silica and gold textures in bonanza ores of the Sleeper Deposit, Humboldt County, Nevada; evidence for colloids and implications for epithermal ore-forming processes. *Econ. Geol.* **89**, 628–638.

Shuster D. L. and Farley K. A. (2005) Diffusion kinetics of proton-induced ^{21}Ne, ^{3}He, and ^{4}He in quartz. *Geochim. Cosmochim. Acta* **69**, 2349–2359.

Shuster D. L., Vasconcelos P. M., Heim J. A. and Farley K. A. (2005) Weathering geochronology by (U-Th)/He dating of goethite. *Geochim. Cosmochim. Acta* **69**, 659–673.

Sillitoe R. H. and Bonham H. F. (1990) Sediment-hosted gold deposits: Distal products of magmatic-hydrothermal systems. *Geology* **18**, 157–161.

Spurr J. E. (1898) *Geology of the Aspen Mining district, Colorado, with Atlas*. US Government Printing Office.

Strutt R. J. (1909) The accumulation of helium in geological time.-II. *Proc. R. Soc. Lond. Ser. A Contain. Pap. Math. Phys. Charact.* **83**, 96–99.

Taksavasu T., Monecke T. and Reynolds T. J. (2018) Textural characteristics of noncrystalline silica in sinters and quartz veins: implications for the formation of bonanza veins in low-sulfidation epithermal deposits. *Minerals* **8**, 331.

Theodore T. G. (2000) Jasperoid along high-angle faults in west-central part of Havallah Hills. In *Geology of Pluton-related Gold Mineralization at Battle Mountain, Nevada: Monographs in Mineral Resource Science No. 2*. Center for Mineral Resources, The University of Arizona, Tucson, pp. 220–222.

Theodore, T.G., Blake, D.W., Loucks, T.A., Johnson, C.A., 1992. Geology of the Buckingham Stockwork Molybdenum Deposit and Surrounding Area, Lander County, Nevada.

Theodore T. G. and Jones G. M. (1991) Geochemistry and Geology of Gold in Jasperoid, Elephant Head Area, Lander County, Nevada. *USGS Bull.* **2009**, 62.

Thompson, W.G., Spiegelman, M.W., Goldstein, S.L., Speed, R. C., 2003. An open-system model for U-series age determinations of fossil corals. 210, 365–381.

Tremblay M. M., Shuster D. L. and Balco G. (2014) Diffusion kinetics of 3He and 21Ne in quartz and implications for cosmogenic noble gas paleothermometry. *Geochim. Cosmochim. Acta* **142**, 186–204.

Vasconcelos P. M., Reich M. and Shuster D. L. (2015) The paleoclimatic signatures of supergene metal deposits. *Elements* **11**, 317–322.

Volk J. A., Lauha E., Leondardson R. W. and Rahn J. E. (1995) Structural geology of the Betze-Post and Meikle deposits, Elko and Eureka counties, Nevada. In *Geology and Ore Deposits of the American Cordillera Symposium Proceedings*. Sparks, Nevada, pp. 142–156.

Waltenberg K. M. (2013) *Mineral Physics and Crystal Chemistry of Minerals Suitable for Weathering Geochronology: Implications to $^{40}Ar/^{39}Ar$ and (U-Th)/He Geochronology*. University of Queensland, Brisbane, Australia.

Wells J. D., Stoiser L. R. and Elliott J. E. (1969) Geology and geochemistry of the Cortez gold deposit, Nevada. *Econ. Geol.* **64**, 526–537.

Wernicke R. S. and Lippolt H. J. (1997) (U+Th)–He evidence of Jurassic continuous hydrothermal activity in the Schwarzwald basement, Germany. *Chem. Geol.* **138**, 273–285.

Wernicke R. S. and Lippolt H. J. (1994a) ^{4}He age discordance and release behavior of a double shell botryoidal hematite from the Schwarzwald, Germany. *Geochim. Cosmochim. Acta* **58**, 421–429.

Wernicke R. S. and Lippolt H. J. (1993) Botryoidal hematite from the Schwarzwald (Germany): heterogeneous uranium distributions and their bearing on the helium dating method. *Earth Planet. Sci. Lett.* **114**, 287–300.

Wernicke R. S. and Lippolt H. J. (1994b) Dating of vein Specularite using internal (U+Th)/^{4}He isochrons. *Geophys. Res. Lett.* **21**, 345–347.

Yigit O., Hofstra A. H., Hitzman M. W. and Nelson E. P. (2006) Geology and geochemistry of jasperoids from the Gold Bar district, Nevada. *Miner. Depos.* **41**, 527–547.

Zeitler P. K., Herczeg A. L., McDougall I. and Honda M. (1987) U-Th-He dating of apatite: A potential thermochronometer. *Geochim. Cosmochim. Acta* **51**, 2865–2868.

Associate editor: David L. Shuster